J. Mech. Phys. Solids 203 (2025) 106174

Contents lists available at ScienceDirect

Journal of the Mechanics and Physics of Solids

journal homepage: www.elsevier.com/locate/jmps

Integrating pulmonary surfactant into lung mechanical simulations: A continuum approach to surface tension in poromechanics

Nibaldo Avilés-Rojas [a,b], Daniel E. Hurtado [a,b,c,*]

[a] Department of Structural and Geotechnical Engineering, School of Engineering, Pontificia Universidad Católica de Chile, Vicuña Mackenna 4860, Santiago, Chile
[b] Institute for Biological and Medical Engineering, Schools of Engineering, Medicine and Biological Sciences, Pontificia Universidad Católica de Chile, Vicuña Mackenna 4860, Santiago, Chile
[c] Institute for Medical Engineering and Science, Massachusetts Institute of Technology, Cambridge, MA, 02140, USA

ARTICLE INFO

Keywords:
Surface tension
Lung compliance
Lung modeling
pressure–volume curve
Internal variables
Pulmonary surfactant
Hysteresis

ABSTRACT

Surface tension arising in the air–liquid interface of alveoli is a fundamental mechanism in lung physiology that explains lung recoil and hysteresis during breathing. However, pulmonary surface tension is typically neglected in continuum models of the lungs, possibly due to their complex multiscale physicochemical nature. In this study, we formulate a poromechanical framework that incorporates the effect of surfactant-dependent surface tension in porous media for the prediction of lung hysteretic response. Using an internal variable formalism, we apply the Coleman–Noll procedure to establish an expression for the stress tensor that includes surface tension akin to the Young–Laplace law. Based on this formulation, we construct a non-linear finite-element model of human lungs to simulate pressure–volume curves and lung response during mechanical ventilation. Our results show that surfactant-dependent surface tension notably modulates pressure–volume curves and lung mechanics. In particular, our model captures the influence of surfactant dynamics on lung hysteresis and compliance, predicting the transition from an insoluble reversible regime to a dissipative one governed by Langmuir kinetics. We envision that our continuum framework will enable lung simulations where surfactant-related phenomena are directly considered in predictions, with important applications to modeling respiratory disease and lung response to mechanical ventilation.

1. Introduction

The lungs are highly porous organs whose mechanical response is fundamental to sustaining life, as they enable the capture of oxygen and the removal of carbon dioxide during respiration. To this end, the lungs undergo cyclic deformations throughout the respiratory cycle, allowing the motion of air in and out. Specifically, air flows from the conduction airways, beginning at the trachea and continuing through the terminal bronchi, then passing through the small airways that extend deep into the lungs, and finally reaching the functional portion of the lungs known as the lung parenchyma. The lung parenchyma is a porous structure that maximizes the surface-to-volume ratio to enable gas exchange. This porous structure comprises millions of units called alveoli, whose cavities (alveolar airspaces) are filled with air that pushes against the alveolar walls. The alveolar walls include a complex network of connective tissue that determines their elasticity and contributes significantly to the structural integrity of the parenchyma (Suki

* Corresponding author at: Department of Structural and Geotechnical Engineering, School of Engineering, Pontificia Universidad Católica de Chile, Vicuña Mackenna 4860, Santiago, Chile.
E-mail address: daniel.hurtado@uc.cl (D.E. Hurtado).

https://doi.org/10.1016/j.jmps.2025.106174
Received 9 January 2025; Received in revised form 1 April 2025; Accepted 1 May 2025
Available online 2 June 2025

et al., 2011). Covering the inner surface of the alveolar walls and in contact with the air is a thin layer of liquid that induces surface tension at the air–liquid interface, which tends to collapse the alveoli (Knudsen and Ochs, 2018). Thus, the mechanical response of parenchyma during breathing is mainly mediated by the elasticity of alveolar walls and the surface tension that results from the air–liquid interface.

The role of surface tension in respiratory function can be attributed mainly to the large pulmonary surface area-to-volume ratio: approximately 85 m^2 of alveolar surface area are contained in the lungs, whose volume is roughly 4 L (West, 2012). In effect, surface forces in the air–liquid interface may account for up to 50% of the elastic recoil, i.e., the tendency to return to its original shape after deformation, in human lungs (Ingenito et al., 2005; v. Neergaard, 1929). One of the most notable features of pulmonary surface tension is its dynamic behavior, where extremely low values are attained to facilitate the breathing process. Such dynamic evolution is explained by the physicochemical activity of the pulmonary surfactant, a complex mixture of proteins and lipids that is adsorbed onto, desorbed from, and squeezed out of the air–liquid interface (Otis et al., 1994; Jbaily et al., 2020). In contrast to clean air–water interfaces, where surface tension has values near 70 dyn/cm, alveolar surface tension varies dynamically during the respiratory cycle. This is due to the ability of surfactant to reduce surface tension, potentially reaching values near 0 dyn/cm during the expiratory phase, avoiding alveolar collapse and allowing normal breathing (Veldhuizen et al., 1998; Scarpelli, 1977). Further, alterations in the metabolism and composition of the surfactant are related to pathological conditions, such as acute respiratory distress syndrome where the abnormally high levels of surface tension cause alveolar collapse, which impedes gas transfer and pulmonary function (Avery and Mead, 1959; Raghavendran et al., 2011; Griese, 1999).

The contribution of alveolar surface tension to lung mechanics has received less attention than the contribution of alveolar wall elasticity, possibly due to its complex multiscale behavior, which depends on the physicochemical nature of surfactant activity and its hysteretic nature. In addition, the effect of the alveolar surfactant-dependent surface tension on the overall lung response is virtually impossible to isolate *in-vivo*, and *in-vitro* approaches have only been able to approximate this contribution by comparing the overall mechanical response of saline-filled lungs, in which surface forces are negligible, with the response of normal air-filled lungs (Mead et al., 1957; Bachofen et al., 1970). In this situation, *in-silico* models arise as a potential tool to improve the understanding of the relation between the alveolar surfactant-dependent surface tension and the organ response. Traditionally, the lung response has been analyzed using compartment models, in which elastic balloons are connected to resistive conduits, allowing a simplified representation of the interaction between the lung parenchyma deformation and the air flowing through the airways (Bates, 2009; Zhou et al., 2021; Morton et al., 2018; Chiew et al., 2018). In these models, the surface tension has been represented by increasing lung compliance, a parameter that represents the ability of the lung to elastically deform and can be estimated experimentally as the slope of the pressure–volume curves (Maury, 2013; Ben-Tal, 2006). To address the spatial distribution of alveolar pressure regional airflow in the lungs, compartment models have been extended towards computational lumped-like fractal models, in which an image-based reconstructed structural airway tree is connected with elastic spherical acinar units whose mechanical response follows empirical equations estimated from quasi-static pressure–volume (P–V) curves (Venegas et al., 1998), see also Neelakantan et al. (2022) for a review on computational lung modeling. Broadly, these models incorporate the contribution of surface tension by stiffening the acinar response by adjusting the parameters of the P–V curves (Middleton et al., 2022) or by adding a collapsing pressure induced by the surface tension (Laplace Law) directly into the equilibrium of the acinar transmural pressure (Ma et al., 2020). Although the latter approach represents the surface tension contribution in the organ response, it lacks kinematic compatibility as discrete acinar units are typically isolated and do not interact with neighboring tissue nor allow for inter-acinar flow.

Poromechanics theory offers a natural continuum framework to represent the interaction arising in neighboring alveolar units and their deformation caused by airflow. Large-strain poroelastic lung models have been formulated to study the 3D distribution of deformation and pressure in idealized dynamic and quasi-static conditions (Berger et al., 2016; Patte et al., 2022). More recently, finite-element simulations based on poromechanical formulations have successfully captured critical physiological variables during mechanical ventilation with clinical relevance (Avilés-Rojas and Hurtado, 2022). Our group also proposed a poroelastic multi-scale finite-deformation framework that takes into account the influence of tissue microstructural properties to predict whole-lung elastic response (Hurtado et al., 2023; Concha and Hurtado, 2020; Concha et al., 2018). Although these poroelastic models offer valuable insights into respiratory mechanics with spatiotemporal resolution, they lack capturing the hysteresis observed during the respiratory cycle, which can be largely attributed to alveolar surface tension. In the last decades, this classical poromechanics framework has been extended to consider elastic surface effects in the interface between the solid matrix and the fluid phases, being applied mainly to the study of differential swelling induced by the adsorption of carbon dioxide in coals during methane production (Vandamme et al., 2010; Zhang, 2018). One of the critical steps in this formulation is the extension of the Helmholtz skeleton free energy potential, adding a term related to the surface energy stored in the matrix–fluid interface. This energy implies an additional stress contribution resulting from the Coleman–Noll procedure, which also considers the geometry of porous media to describe the interface. In addition, surface forces at the interface depend on the adsorption process, resulting in a stress tensor that depends on the concentration of the adsorbed compound. These models constitute a starting point to obtain a representative expression of alveolar stress in a thermodynamically consistent way. However, the applicability of this approach to modeling biological tissues, and the lung parenchyma in particular, poses the challenge of incorporating hysteretical behavior that results from internal non-equilibrium processes such as the dynamic adsorption and desorption of pulmonary surfactant, which has not been addressed to date.

In this work, we propose a continuum framework for lung parenchyma mechanics that incorporates the surfactant-dependent surface tension in alveoli, allowing us to predict the hysteretic response of lungs. To this end, we formulate a continuum poromechanical framework with surface effects in which the air–liquid interface surfactant concentration directly modulates the

surface tension. A novel aspect of this formulation is the consideration of the surface tension in continuum whole lung mechanics modeling. This paper is organized as follows. In Section 2, we formulate our lung model, starting with the balance laws and thermodynamic restrictions governing porous media mechanics. Next, considering an internal variable framework to track the surfactant mass evolution, we apply the Coleman–Noll procedure to find a general constitutive relationship for the stress tensor representing the lung parenchyma response. This relationship is particularly developed for pulmonary alveoli, represented by a spherical shell geometry and a known surfactant model. Strong and weak formulations of this problem are also introduced. Nonlinear finite-element discretizations of the weak formulation are further constructed to simulate pressure–volume curves during supersyringe tests and mechanical ventilation therapy, whose details and results are presented in Section 3. Finally, in Section 4, we discuss our model formulation and its advantages over state-of-the-art virtual lungs.

2. Modeling of lung mechanics with alveolar surface tension effects

To model the effect of surface tension in the lung, we adopt a multiscale approach where each point in the continuum domain will contain interacting phases at the microstructural level, see Fig. 1 for a schematic. The lung parenchyma domain is composed of the alveolar structure and the alveolar airspace. The alveolar structure is partitioned into the connective tissue and the liquid lining layer that covers the alveolar walls, see inset in Fig. 1. Further, we assume that the liquid lining layer contains surfactant in its bulk solution and on the airspace interface. Moreover, the alveolar airspace is assumed to be fully filled with air that flows throughout the lung domain.

Due to its physicochemical behavior, the surfactant can undergo dynamic processes of adsorption and desorption within the liquid lining layer subsystem, i.e., between its bulk solution and its interface with the air. For simplicity, we will assume that the liquid lining layer in one alveolar unit is not connected with other alveolar units, so that surfactant cannot be transported across the lung parenchyma. Under this assumption, the lining liquid layer can be assumed to be attached to the alveolar tissue, allowing us to consider them as a single phase. Based on these definitions, the lung parenchyma can be described as a two-phase saturated porous medium with air and structural phases. We note that the surfactant dynamics within the alveolar structure will be represented as an internal process governed by thermodynamic considerations, as described below.

2.1. Kinematics and balance laws in the lung parenchyma

Considering a continuum framework (Coussy, 2004), we assume that an infinitesimal element of parenchyma and air coincide at a macroscopic current point $\boldsymbol{x}$, see Fig. 1. The Lagrangian observer follows the deformation of the parenchyma and not of the air, so that the current (Eulerian) configuration at a time t is defined as $\Omega = \boldsymbol{\varphi}(\Omega_R, t)$, where Ω_R is the parenchyma reference (Lagrangian) configuration and $\boldsymbol{\varphi} : \Omega_R \times \mathbb{R} \to \mathbb{R}^3$ is the deformation mapping. The deformation-gradient tensor field $\boldsymbol{F} : \Omega_R \times \mathbb{R} \to \mathbb{R}^{3\times 3}$ is defined as $\boldsymbol{F} := \mathrm{Grad}\boldsymbol{\varphi}(\boldsymbol{X}, t)$ where $\boldsymbol{X}$ is the position of a point in the parenchyma at the reference configuration, and Grad represents the gradient of a field with respect to the reference configuration coordinates. Let $d\Omega$ be the volume in the current configuration of an infinitesimal volume and $d\Omega_R$ its corresponding infinitesimal volume in the reference configuration. Then, the Jacobian field $J : \Omega_R \times \mathbb{R} \to \mathbb{R}$ is defined as $J := d\Omega/d\Omega_R = \det \boldsymbol{F}$. Further, we introduce the Green–Lagrange strain tensor $\boldsymbol{E} : \Omega_R \times \mathbb{R} \to \mathbb{R}^{3\times 3}$ as

$$\boldsymbol{E} := \frac{1}{2}\left(\boldsymbol{F}^T\boldsymbol{F} - \boldsymbol{I}\right), \tag{1}$$

where $\boldsymbol{I}$ is the Identity tensor. The Eulerian porosity field $\phi : \Omega \times \mathbb{R} \to \mathbb{R}$ is defined as the fraction of current air volume $d\Omega^a$ over the overall current infinitesimal volume, that is, $\phi := d\Omega^a/d\Omega$. Then, the air volume at a current point $\boldsymbol{x}$ is $\phi d\Omega$, and the volume of the alveolar structure is $(1-\phi)\,d\Omega$. We also define the Lagrangian porosity field $\boldsymbol{\Phi} : \Omega_R \times \mathbb{R} \to \mathbb{R}$ as $\boldsymbol{\Phi} := d\Omega^a/d\Omega_R$, and we note that these two porosity fields are related through the relation $\boldsymbol{\Phi} = J(\phi \circ \boldsymbol{\varphi})$ Coussy (2004), where $\circ$ represents function composition, i.e., $(\phi \circ \boldsymbol{\varphi})(\boldsymbol{X}, t) := \phi(\boldsymbol{\varphi}(\boldsymbol{X}, t))$.

Conservation laws are naturally formulated in the current configuration. Let $\rho_a : \Omega \times \mathbb{R} \to \mathbb{R}$ and $\rho_s : \Omega \times \mathbb{R} \to \mathbb{R}$ be the air and alveolar structure current density fields, respectively. Further, let $\boldsymbol{v}_a : \Omega \times \mathbb{R} \to \mathbb{R}^3$ be the current air velocity field and $\boldsymbol{v}_s : \Omega \times \mathbb{R} \to R^3$ the current alveolar structure velocity field. Mass conservation for the airspace and alveolar structure are then governed by the expressions

$$\frac{\partial(\rho_a\phi)}{\partial t} + \mathrm{div}(\rho_a\phi\boldsymbol{v}_a) = 0 \quad \text{in } \Omega \times \mathbb{R}, \tag{2}$$

$$\frac{\partial(\rho_s(1-\phi))}{\partial t} + \mathrm{div}(\rho_s(1-\phi)\boldsymbol{v}_s) = 0 \quad \text{in } \Omega \times \mathbb{R}, \tag{3}$$

respectively, where div represents the divergence operator of a field with respect to the current configuration coordinates. We further define the filtration airflow vector field $\boldsymbol{q} : \Omega \times \mathbb{R} \to \mathbb{R}^3$ as

$$\boldsymbol{q} := \phi(\boldsymbol{v}_a - \boldsymbol{v}_s). \tag{4}$$

Then, one can show that air mass conservation expressed relative to the movement of the alveolar structure reads

$$\frac{\partial(\rho_a\phi)}{\partial t} + \mathrm{grad}(\rho_a\phi)\cdot\boldsymbol{v}_s + \rho_a\phi\,\mathrm{div}\,\boldsymbol{v}_s + \mathrm{div}(\rho_a\boldsymbol{q}) = 0 \quad \text{in } \Omega \times \mathbb{R}, \tag{5}$$

where grad represents the gradient operator of a field with respect to the current configuration coordinates. Let $\boldsymbol{\sigma} : \Omega \times \mathbb{R} \to \mathbb{R}^{3\times 3}$ be the Cauchy stress tensor for the composite medium, $\boldsymbol{b} : \Omega \times \mathbb{R} \to \mathbb{R}^3$ the current body force density, $\boldsymbol{a}_a : \Omega \times \mathbb{R} \to \mathbb{R}^3$ the current

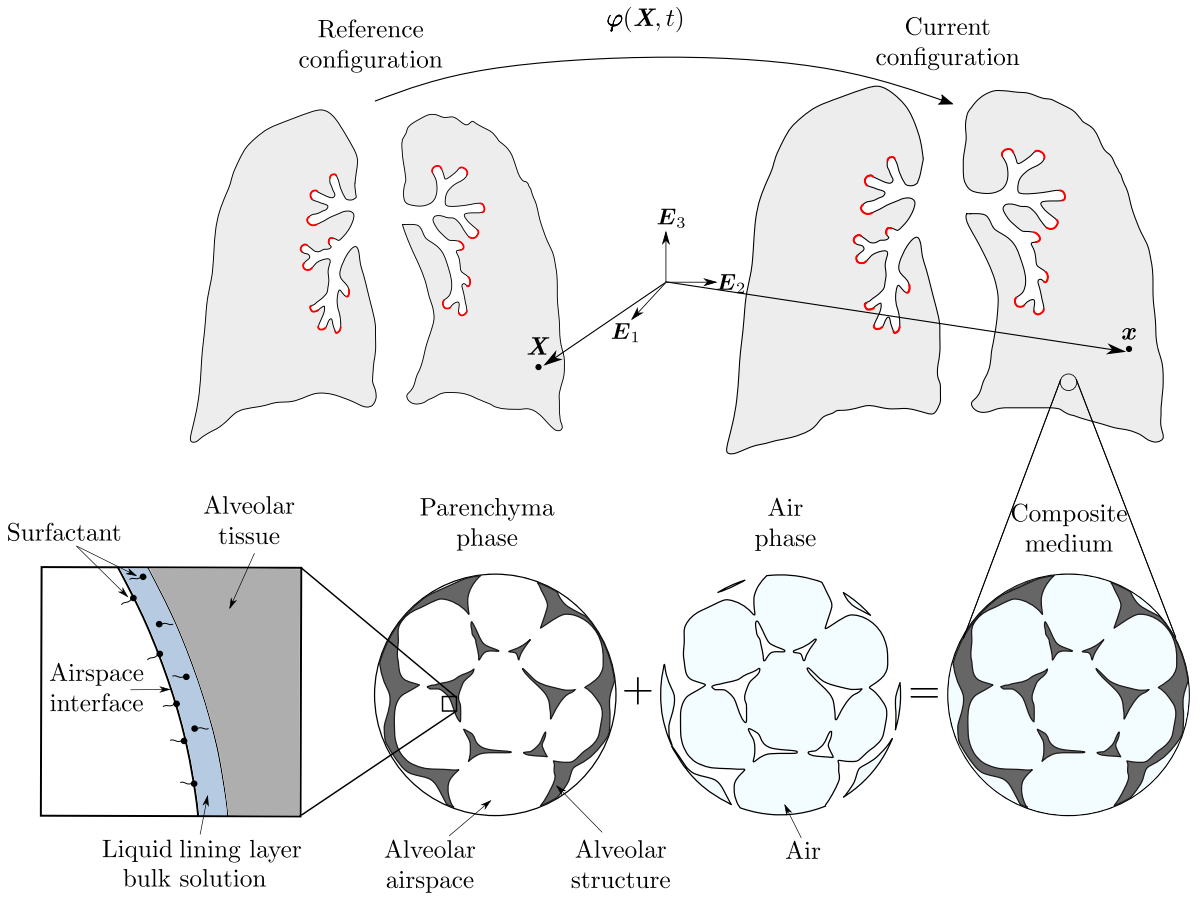

Fig. 1. Multiscale approach to model surface tension effects in the lung parenchyma. Lung tissue is idealized as a continuum in which an infinitesimal element of parenchyma and air coexist in a point $\boldsymbol{x}$ of the current configuration. Lung parenchyma comprises the alveolar structure and alveolar airspace. The alveolar structure is partitioned into the connective tissue and the liquid lining layer that contains surfactant in its bulk solution and on the interface with the air.

acceleration field for the air phase, and $\boldsymbol{a}_s : \Omega\times\mathbb{R}\to\mathbb{R}^3$ the current acceleration field for the alveolar structure phase. Then, linear momentum balance reads

$$\mathrm{div}\boldsymbol{\sigma} + \rho_s(1-\phi)(\boldsymbol{b}-\boldsymbol{a}_s) + \rho_a\phi(\boldsymbol{b}-\boldsymbol{a}_a) = 0 \quad \text{in } \Omega\times\mathbb{R}. \tag{6}$$

We will be interested in expressing all governing balance laws in the reference configuration. To this end, we consider the pull-back of the filtration airflow vector field $\boldsymbol{Q} : \Omega_R\times\mathbb{R}\to\mathbb{R}^3$, which, by standard arguments, takes the form

$$\boldsymbol{Q} = J(\boldsymbol{F}^{-1}\boldsymbol{q})\circ\boldsymbol{\varphi}. \tag{7}$$

Then, the pull-back of the air mass balance Eq. (5) reads

$$\frac{\partial\left((\rho_a\circ\boldsymbol{\varphi})\boldsymbol{\Phi}\right)}{\partial t} + \mathrm{Div}\left((\rho_a\circ\boldsymbol{\varphi})\boldsymbol{Q}\right) = 0 \quad \text{in } \Omega_R\times\mathbb{R}, \tag{8}$$

where Div represents the divergence operator of a field with respect to the reference configuration coordinates. Further, assuming the air phase is incompressible (Hurtado et al., 2023), (8) simplifies to

$$\frac{\partial\boldsymbol{\Phi}}{\partial t} + \mathrm{Div}\boldsymbol{Q} = 0 \quad \text{in } \Omega_R\times\mathbb{R}. \tag{9}$$

The mass balance law for the structural matrix is straightforward because its mass is constant, and reads

$$\frac{\partial\left((\rho_s\circ\boldsymbol{\varphi})(J-\boldsymbol{\Phi})\right)}{\partial t} = 0 \quad \text{in } \Omega_R\times\mathbb{R}. \tag{10}$$

We note that in writing (10), we do not restrict mass exchange processes within the alveolar structure, such as those we will consider for pulmonary surfactant later. To obtain a reference form of the linear momentum balance, we define the second Piola–Kirchhoff stress tensor field $\boldsymbol{S} : \Omega_R\times\mathbb{R}\to\mathbb{R}^{3\times3}$ as

$$\boldsymbol{S} = J\boldsymbol{F}^{-1}\boldsymbol{\sigma}\boldsymbol{F}^{-T}. \tag{11}$$

Then, by pulling back (6) and neglecting inertial terms, the reference form of the conservation of linear momentum reads

$$\mathrm{Div}\,(\boldsymbol{F}\boldsymbol{S}) + R\boldsymbol{B} = 0 \quad \text{in } \Omega_R \times \mathbb{R}, \tag{12}$$

where $\boldsymbol{B} := \boldsymbol{b}\circ\boldsymbol{\varphi}$, $R := J(\rho\circ\boldsymbol{\varphi})$ with $\rho := (1-\phi)\rho_s + \phi\rho_a$.

2.2. Thermodynamics of tissue mechanics and surfactant dynamics

To ensure thermodynamic consistency in our poromechanical framework, we consider the parenchyma Helmholtz free energy (per unit of reference volume) function Ψ_{par} and we write the Clausius–Duhem inequality for an isothermal porous medium as (Coussy, 2004)

$$\left(\boldsymbol{S} : \dot{\boldsymbol{E}} + P_{\mathrm{alv}}\dot{\Phi} - \dot{\Psi}_{\mathrm{par}}\right) + \left(-\mathrm{Grad}(P_{\mathrm{alv}}) + \rho_a \boldsymbol{F}^T\boldsymbol{B}\right)\cdot\boldsymbol{Q} \geq 0, \tag{13}$$

in which we have assumed that there are no chemical interactions between air and structural alveolar phases, and where $P_{\mathrm{alv}} : \Omega_R \times \mathbb{R} \to \mathbb{R}$ is the air pressure field. We further note that the dot on a field indicates the total time (material) derivative. Eq. (13) considers an open system for the air phase and a closed system for the alveolar structure. In addition, the first and second terms in (13) represent the energy dissipation that takes place in the parenchyma and in the air phase due to viscous airflow. Due to the highly distinct nature of the dissipation terms, we assume that we can separate (13) into two inequalities, one per phase, which read

$$\mathcal{D}_{\mathrm{air}} = \left(-\mathrm{Grad}(P_{\mathrm{alv}}) + \rho_a \boldsymbol{F}^T\boldsymbol{B}\right)\cdot\boldsymbol{Q} \geq 0, \tag{14}$$

$$\mathcal{D}_{\mathrm{par}} = \boldsymbol{S} : \dot{\boldsymbol{E}} + P_{\mathrm{alv}}\dot{\Phi} - \dot{\Psi}_{\mathrm{par}} \geq 0. \tag{15}$$

where $\mathcal{D}_{\mathrm{air}}$ is the energy dissipation related to the viscous airflow, and $\mathcal{D}_{\mathrm{air}}$ is the energy dissipation associated with parenchyma. We note that Eq. (14) imposes a thermodynamic restriction on the constitutive law for airflow. A standard way to ensure its positivity is to consider a quadratic dissipation form, which leads to the classical Darcy's law (Choo, 2018),

$$\boldsymbol{Q} = \frac{1}{\eta} J\boldsymbol{F}^{-1}\boldsymbol{\kappa}\boldsymbol{F}^{-T}\left[-\mathrm{Grad}(P_{\mathrm{alv}}) + \rho_a\boldsymbol{F}^T\boldsymbol{B}\right], \tag{16}$$

where $\boldsymbol{\kappa}$ is the intrinsic permeability tensor, that for a medium with isotropic flow behavior reads $\boldsymbol{\kappa} = \kappa\boldsymbol{I}$ with κ the isotropic intrinsic permeability; and η is the dynamic viscosity of the air. Similarly, Eq. (15) restricts the constitutive relation for the parenchyma, and we note that Ψ_{par} admits as natural arguments the state variables $\boldsymbol{E}$, Φ, in addition to internal variables that govern internal processes. Based on the high water percentage in the alveolar tissue and the liquid lining layer (Lange and Schuster, 1999), we will assume that the alveolar structure is incompressible. Then, it follows that the Lagrangian porosity field Φ depends on the Jacobian, such that the following relationship holds (Coussy, 2004)

$$J = 1 + \Phi - \Phi_R \tag{17}$$

where Φ_R is the reference Lagrangian porosity. Replacing this expression in (15) and using the identity

$$\dot{J} = J\boldsymbol{F}^{-1}\boldsymbol{F}^{-T} : \dot{\boldsymbol{E}}, \tag{18}$$

we rewrite the parenchyma dissipation inequality (15) as

$$\mathcal{D}_{\mathrm{par}} = \boldsymbol{S} : \dot{\boldsymbol{E}} + P_{\mathrm{alv}}J\boldsymbol{F}^{-1}\boldsymbol{F}^{-T} : \dot{\boldsymbol{E}} - \dot{\Psi}_{\mathrm{par}} \geq 0. \tag{19}$$

To consider the surfactant-dependent surface tension in our formulation, we will postulate the existence of a parenchyma Helmholtz free energy Ψ_{par} that can split into the classical hyperelastic energy Ψ^{el} associated with the alveolar tissue and the airspace, and into energy Ψ^{st} related to the surface tension that results from surfactant interactions within the liquid lining layer subsystem (Vandamme et al., 2010)

$$\Psi_{\mathrm{par}} := \Psi^{\mathrm{el}} + \Psi^{\mathrm{st}}. \tag{20}$$

Due to the additive nature of the Helmholtz free energy, we also assume the decomposition (Zhao et al., 2021)

$$\Psi^{\mathrm{st}} := \Psi^{\mathrm{st}}_{\mathrm{surf}} + \Psi^{\mathrm{st}}_{\mathrm{bulk}}, \tag{21}$$

where $\Psi^{\mathrm{st}}_{\mathrm{surf}}$ is the surface energy stored in the airspace interface, and $\Psi^{\mathrm{st}}_{\mathrm{bulk}}$ is the energy contribution of the surfactant bulk solution. To incorporate the surfactant exchange (adsorption–desorption) between the bulk solution and the airspace interface, we introduce the interfacial surfactant mass density $M_{\mathrm{surf}} : \Omega_R \times \mathbb{R} \to \mathbb{R}$, defined as $M_{\mathrm{surf}} := d\mathcal{M}_{\mathrm{surf}}/d\Omega_R$, with $d\mathcal{M}_{\mathrm{surf}}$ the mass of (adsorbed) surfactants that covers the airspace interface in an infinitesimal current volume; and $M_{\mathrm{bulk}} : \Omega_R \times \mathbb{R} \to \mathbb{R}$ the bulk solution surfactant mass density, whose definition is analogous to M_{surf}.[1] In addition, to consider effects of area changes over the energy Ψ^{st}, we define

[1] Alternatively, our framework can be expressed using the number of surfactant molecules instead of surfactant mass. However, we choose to use surfactant mass because of the available constitutive equations and parameters for pulmonary surfactants.

the interfacial area density $A : \Omega_R \times \mathbb{R} \to \mathbb{R}$ as $A := d\mathcal{A}/d\Omega_R$, where $d\mathcal{A}$ is the current area of airspace interface in the deformed infinitesimal volume. We remark that implicit in our internal variable framework, the airspace interface and the bulk solution are described by their mean values, neglecting fluctuations within them. Then, we will assume the validity of the thermodynamic Gibbs relations, and using previous definitions, we can write the energy balance for both components of the liquid lining layer subsystem. For the case of the airspace interface, we consider the extensive properties A and M_{surf} as natural variables for its Helmholtz free energy. Thus, the energy balance for the airspace interface includes the work related to changes in the airspace interfacial area and the energy associated with changes in the interfacial surfactant mass and reads (Vandamme et al., 2010; Butt et al., 2023)

$$\mathrm{d}\Psi^{\text{st}}_{\text{surf}} = \gamma \mathrm{d}A + \mu_{\text{surf}} \mathrm{d}M_{\text{surf}}, \tag{22}$$

in which γ is the airspace surface tension and μ_{surf} is the (mass-based) chemical potential of the surfactants in the airspace interface. From Eq. (22) we can define the airspace surface tension as the partial derivative of the surface Helmholtz free energy with respect to the interfacial area density (Kralchevsky et al., 1997)

$$\gamma := \frac{\partial \Psi^{\text{st}}_{\text{surf}}}{\partial A}, \tag{23}$$

while its partial derivative concerning the interfacial mass gives the chemical potential

$$\mu_{\text{surf}} := \frac{\partial \Psi^{\text{st}}_{\text{surf}}}{\partial M_{\text{surf}}}. \tag{24}$$

In the case of the bulk solution, M_{bulk} is regarded as a natural variable of its corresponding Helmholtz free energy, allowing us to express the energy balance for the bulk solution as

$$\mathrm{d}\Psi^{\text{st}}_{\text{bulk}} = \mu_{\text{bulk}} \mathrm{d}M_{\text{bulk}}, \tag{25}$$

where volume-work contribution has been neglected and μ_{bulk} is the chemical potential of surfactants in the bulk solution, which is different from μ_{surf} for a non-equilibrium state, and that can be obtained from the bulk free energy as

$$\mu_{\text{bulk}} := \frac{\partial \Psi^{\text{st}}_{\text{bulk}}}{\partial M_{\text{bulk}}}. \tag{26}$$

Concerning the surface tension defined in (23), it is important to mention that, in the context of surface thermodynamics, it is common to expand the surface tension γ as

$$\gamma = \gamma_0 - \Pi, \tag{27}$$

where γ_0 is the surface tension of the airspace interface free of surfactants, tending to reduce the interfacial area; and Π is the surface pressure of the surfactant, which acts in the opposite way (Manikantan and Squires, 2020). This expression arises from splitting $\Psi^{\text{st}}_{\text{surf}}$ into an energetic term related to the surfactant-free airspace interface and another term related to the surfactant film at the interface (Zhang et al., 2014).

Since the surfactant mass exchange is an internal process in the parenchyma, M_{surf} and M_{bulk} can be related through the mass conservation of surfactant in an infinitesimal volume, that reads

$$M_{\text{surf}} + M_{\text{bulk}} = \text{constant} \tag{28}$$

and we note that the total differential of the surfactant bulk mass density in (25) can be rewritten as $\mathrm{d}M_{\text{bulk}} = -\mathrm{d}M_{\text{surf}}$. Furthermore, considering the incompressibility of the alveolar structure phase and neglecting pore-scale mechanisms, we assume that variations in A are completely defined by the Green–Lagrange strain tensor. Then, we conclude that the parenchyma Helmholtz free energy has as arguments $\boldsymbol{E}$ and M_{surf}, which corresponds to an *internal variable* for the parenchyma energy dissipation. Based on this physicochemical microstructural nature, we define the Helmholtz free energies related to the airspace interface and the surfactant bulk solution as

$$\Psi^{\text{st}}_{\text{surf}} := \Psi^{\text{st}}_{\text{surf}}\left(A(\boldsymbol{E}), M_{\text{surf}}\right), \quad \Psi^{\text{st}}_{\text{bulk}} := \Psi^{\text{st}}_{\text{bulk}}\left(M_{\text{bulk}}(M_{\text{surf}})\right) \tag{29}$$

respectively, where $\Psi^{\text{st}}_{\text{surf}}$ depends on the Green–Lagrange strain tensor $\boldsymbol{E}$ through the interfacial area density A and on the interfacial surfactant mass density M_{surf}; and $\Psi^{\text{st}}_{\text{bulk}}$ only is a function of M_{surf} through the bulk solution surfactant mass density M_{bulk}. Note that the bulk solution energy $\Psi^{\text{st}}_{\text{bulk}}$ does not depend on $\boldsymbol{E}$ mainly due to the incompressibility assumption of the alveolar structure. In a more general case, the energy balance (25) has to include a volume-work term, and the bulk solution energy $\Psi^{\text{st}}_{\text{bulk}}$ should also depend on the parenchyma deformations through the current volume of the bulk solution. Following a standard Coleman–Noll procedure (Coleman, 1964; Coleman and Gurtin, 1967), we proceed with the calculation of the total derivative of the Helmholtz free energy Ψ_{par}, which, applying the chain rule, result in

$$\dot{\Psi}_{\text{par}} = \frac{\partial \Psi^{\text{el}}}{\partial \boldsymbol{E}} : \dot{\boldsymbol{E}} + \frac{\partial \Psi^{\text{st}}_{\text{surf}}}{\partial A}\frac{\partial A}{\partial \boldsymbol{E}} : \dot{\boldsymbol{E}} + \frac{\partial \Psi^{\text{st}}_{\text{surf}}}{\partial M_{\text{surf}}}\dot{M}_{\text{surf}} + \frac{\partial \Psi^{\text{st}}_{\text{bulk}}}{\partial M_{\text{bulk}}}\frac{\partial M_{\text{bulk}}}{\partial M_{\text{surf}}}\dot{M}_{\text{surf}}. \tag{30}$$

Using definitions (23), (24), (26) and noting from Eq. (28) that $\partial M_{\text{bulk}}/\partial M_{\text{surf}} = -1$, the total derivative (30) is rewritten as

$$\dot{\Psi}_{\text{par}} = \left(\frac{\partial \Psi^{\text{el}}}{\partial \boldsymbol{E}} + \gamma \frac{\partial A}{\partial \boldsymbol{E}}\right) : \dot{\boldsymbol{E}} + \mathcal{L}\,\dot{M}_{\text{surf}}, \tag{31}$$

where we have defined the thermodynamic force conjugated with the rate $\dot{M}_{\text{surf}}$ as

$$\mathcal{L} := \mu_{\text{surf}} - \mu_{\text{bulk}}. \tag{32}$$

We remark that from a macroscopic perspective, such as the one considered in this work, the terms μ_{surf} and μ_{bulk} should be interpreted as *internal* chemical potentials because they describe internal interactions within the liquid lining layer subsystem, and not the interaction with other matter such as the air phase (Lu and Zhang, 2019). Grouping terms and replacing (31) in (19), the following thermodynamic inequality arises

$$\mathcal{D}_{\text{par}} = \left(\boldsymbol{S} + P_{\text{alv}} J \boldsymbol{F}^{-1} \boldsymbol{F}^{-T} - \gamma \frac{\partial A}{\partial \boldsymbol{E}} - \frac{\partial \Psi^{\text{el}}}{\partial \boldsymbol{E}} \right) : \dot{\boldsymbol{E}} - \mathcal{L} \dot{M}_{\text{surf}} \geq 0. \tag{33}$$

We note that Eq. (33) is similar to the Clausius–Duhem inequality for a poromechanical medium with incompressible solid matrix without interfacial effects (Coussy, 2004), plus a term opposite to the pore pressure that takes into account the surface tension; and a dissipative term due to dynamic of the surfactant. In view of classical continuum mechanics arguments (Coleman, 1964; Coleman and Gurtin, 1967), the inequality (33) must be satisfied for an arbitrary choices of $\dot{\boldsymbol{E}}$, and we deduce the constitutive equation

$$\boldsymbol{S} = \frac{\partial \Psi^{\text{el}}}{\partial \boldsymbol{E}} + \gamma \frac{\partial A}{\partial \boldsymbol{E}} - P_{\text{alv}} J \boldsymbol{F}^{-1} \boldsymbol{F}^{-T}. \tag{34}$$

Furthermore, in our formulation the reference configuration satisfies $\boldsymbol{S} = 0$, $P_{\text{alv}} = 0$ and $M_{\text{surf}} = M^R_{\text{surf}}$ when $\boldsymbol{E} = \boldsymbol{I}$, with M^R_{surf} the reference interfacial surfactant mass. In assuming these conditions for the reference configuration, we note that the surfactant at the airspace interface cancels the surface tension from water, see also expression (27), and therefore M^R_{surf} must be chosen such that $\gamma = 0$. Using (34), the dissipative potential due to non-equilibrium internal surfactant interactions remains

$$\mathcal{D}_{\text{par}} = -\mathcal{L} \dot{M}_{\text{surf}} \geq 0. \tag{35}$$

In Eq. (35), the term $\dot{M}_{\text{surf}}$ must provide an *evolution law* for the interfacial surfactant mass in the form of a differential equation

$$\dot{M}_{\text{surf}} = \mathcal{F}, \tag{36}$$

where $\mathcal{F}$ is a term defined by chosen surfactant material model. We remark that the first and second terms of (34) are related to the main recoil mechanisms of the lung, named the tissue elasticity and the alveolar surface tension, which is one of the essential contributions of this work.

To provide a specific expression of the stress tensor $\boldsymbol{S}$, we need to compute the geometrical factor $\partial A / \partial \boldsymbol{E}$ in Eq. (34), which accounts for alveolar surface-area changes during deformation processes. To this end, we consider a single-alveolus structure, which we represent by a spherical shell with internal and external radii in the reference configuration denoted by fields $\mathcal{R}_{RI} : \Omega_R \to \mathbb{R}$ and $\mathcal{R}_{RE} : \Omega_R \to \mathbb{R}$, respectively. In this geometrical model, the airspace interface corresponds to the surface defined by the inner spherical domain. Using basic geometric relationships, the overall reference volume, the reference air volume, and the reference Lagrangian porosity for this microstructure can be expressed by $d\Omega_R = (4/3)\pi \mathcal{R}^3_{RE}$, $d\Omega^a_R = (4/3)\pi \mathcal{R}^3_{RI}$, and

$$\Phi_R = \frac{\mathcal{R}^3_{RI}}{\mathcal{R}^3_{RE}}, \tag{37}$$

respectively. Furthermore, let $r_i : \Omega \times \mathbb{R} \to \mathbb{R}$ and $r_r : \Omega \times \mathbb{R} \to \mathbb{R}$ the deformed inner and outer radii, respectively, that are written in the reference configuration as $\mathcal{R}_i = r_i \circ \boldsymbol{\varphi}$ and $\mathcal{R}_e = r_e \circ \boldsymbol{\varphi}$. In a similar way that references volumetric relationships, the overall infinitesimal volume, air volume, and Lagrangian porosity field of the deformed microstructure are written as $d\Omega = (4/3)\pi \mathcal{R}^3_e$, $d\Omega^a = (4/3)\pi \mathcal{R}^3_i$ and

$$\Phi = \frac{\mathcal{R}^3_i}{\mathcal{R}^3_{RE}}, \tag{38}$$

respectively. The interfacial area also can be written as a function of the internal radius of the deformed sphere as $d\mathcal{A} = 4\pi \mathcal{R}^2_i$. Then, the interfacial area density is $A = 3\mathcal{R}^2_i / \mathcal{R}^3_{RE}$, which using (37) and (38), can be rewritten as (Zhang, 2018)

$$A = \frac{3}{\mathcal{R}_{RI}} \Phi_R^{1/3} \Phi^{2/3}. \tag{39}$$

Through the chain rule, we can compute

$$\frac{\partial A}{\partial \boldsymbol{E}} = \frac{\partial A}{\partial \Phi} \frac{\partial \Phi}{\partial \boldsymbol{E}} = \frac{2}{\mathcal{R}_{RI}} \left(\frac{\Phi_R}{\Phi} \right)^{1/3} J \boldsymbol{F}^{-1} \boldsymbol{F}^{-T} \tag{40}$$

where we had used the identity

$$\frac{\partial \Phi}{\partial \boldsymbol{E}} = J \boldsymbol{F}^{-1} \boldsymbol{F}^{-T}. \tag{41}$$

Finally, replacing (40) into (34) the total stress tensor is expressed as

$$\boldsymbol{S} = \frac{\partial \Psi^{\text{el}}}{\partial \boldsymbol{E}} + P_\gamma J \boldsymbol{F}^{-1} \boldsymbol{F}^{-T} - P_{\text{alv}} J \boldsymbol{F}^{-1} \boldsymbol{F}^{-T}, \tag{42}$$

where

$$P_\gamma := \frac{2\gamma}{\mathcal{R}_{RI}}\left(\frac{\Phi_R}{\Phi}\right)^{1/3} \tag{43}$$

is the collapse pressure due to the surface tension. In this term we note that for a given values of reference external radius $\mathcal{R}_{RE}$ and reference Lagrangian porosity Φ_R, and considering (37) we can write $\mathcal{R}_{RI} := \mathcal{R}_{RI}(\Phi_R, \mathcal{R}_{RE})$ and choose $\mathcal{R}_{RE}$ and Φ_R as geometrical parameters of the model.

2.3. Constitutive models for parenchymal tissue and surfactant

To close our formulation, specific constitutive models for tissue and surfactant are needed. In the case of pulmonary tissue, for simplicity, we adopt an exponential-like material model with an energy density function that reads (Fung et al., 1978; Tawhai et al., 2009; Ma et al., 2013)

$$\Psi^{\text{el}} = c\left[\exp\left(aJ_1^2 + bJ_2\right) - 1\right], \tag{44}$$

where a, b, c are material parameters, and J_1, J_2 are the first and second invariant of the Green–Lagrange strain tensor $\boldsymbol{E}$, i.e.,

$$J_1 := \text{tr}\boldsymbol{E}, \quad J_2 := \frac{1}{2}\left[(\text{tr}\boldsymbol{E})^2 - \text{tr}\boldsymbol{E}^2\right]. \tag{45}$$

In the case of pulmonary surfactant, to the best of our knowledge, there are currently no Helmholtz free energy expressions Ψ^{st} suitable for the complex behavior of pulmonary surfactants. We also note that traditional model for surfactants, such as the Langmuir or the Frumkin models, do not consider the phase changes observed in pulmonary surfactants. Furthermore, it is known that in these expressions, surface tension diverges for high interfacial surfactant concentration (Manikantan and Squires, 2020), not allowing surface tensions to decrease their magnitude near zero, a behavior typically observed in pulmonary alveoli. Based on these limitations, we adopt the adsorption-limited model proposed by Otis et al. (1994) and integrate it into our continuum poromechanical framework. This surfactant model has three phases whose thresholds are defined regarding the interfacial surfactant concentration Γ, defined as

$$\Gamma := \frac{\boldsymbol{M}_{\text{surf}}}{A}. \tag{46}$$

We introduce the material parameter Γ_∞, named the maximum equilibrium interfacial concentration, to define these regimes. For concentration less than Γ_∞, surfactant can be adsorbed at the interface or desorbed from it, according to the Langmuir non-equilibrium kinetics. For concentrations between Γ_∞ and the maximum dynamic concentration $\Gamma_{\max}$ (tightly packing possible), the surfactant behaves as an insoluble compound in which there is no surfactant mass exchange, and any changes in interfacial concentration are only due to changes in the area. When $\Gamma = \Gamma_{\max}$, any area reduction results in the squeeze out of interfacial surfactant to the bulk. For this three-phase model, the term $\mathcal{F}$ in Eq. (36) is written as

$$\mathcal{F} = \begin{cases} A\left(k_1 C\left(\Gamma_\infty - \Gamma\right) - k_2\Gamma\right) & \text{if} \quad \Gamma < \Gamma_\infty, \\ 0 & \text{if} \quad \{\Gamma_\infty \le \Gamma < \Gamma_{\max}\} \text{ or } \{\Gamma = \Gamma_{\max} \text{ and } \dot{A} \ge 0\}, \\ \Gamma_{\max}\dot{A} & \text{if} \quad \Gamma = \Gamma_{\max} \quad \text{and} \quad \dot{A} < 0, \end{cases} \tag{47}$$

where k_1, k_2, and C are material parameters that represent the adsorption coefficient, desorption coefficient, and bulk surfactant concentration, respectively. We note that the deformation-rate dependence of the squeeze-out regime represents a reversible evolution of the internal variable in this regime (Lubliner, 1973). To prevent an additional stress term in Eq. (34), we will neglect the force $\mathcal{L}$ for the stress calculation during this regime. We further write the surface tension γ as the piecewise function,

$$\gamma = \begin{cases} \gamma_0 - m_1\left(\dfrac{\Gamma}{\Gamma_\infty}\right) & \text{if} \quad \Gamma < \Gamma_\infty, \\ \gamma_\infty - m_2\left(\dfrac{\Gamma}{\Gamma_\infty} - 1\right) & \text{if} \quad \{\Gamma_\infty \le \Gamma < \Gamma_{\max}\} \text{ or } \{\Gamma = \Gamma_{\max} \text{ and } \dot{A} \ge 0\}, \\ \gamma_{\min} & \text{if} \quad \Gamma = \Gamma_{\max} \quad \text{and} \quad \dot{A} < 0, \end{cases} \tag{48}$$

with m_1 the slope of the Langmuir regime isotherm; m_2 the slope of the insoluble regime isotherm; γ_∞ the surface tension corresponding to Γ_∞; and $\gamma_{\min}$ the minimum surface tension that occurs when the dynamic maximum concentration $\Gamma_{\max}$ is reached. Note from (47) that during the Langmuir regime, the interfacial concentration for a stationary process ($\mathcal{F} = 0$) tends to the value

$$\Gamma_{\text{eq}} = \left(\frac{k_1 C}{k_1 C + k_2}\right)\Gamma_\infty. \tag{49}$$

and surface tension during this regime also tends to the equilibrium surface tension defined as $\gamma_{\text{eq}} := \gamma(\Gamma_{\text{eq}})$. Further, we note that for given material parameters Γ_∞, γ_0, $\gamma_{\min}$, m_1, m_2, we can write

$$\gamma_\infty = \gamma_0 - m_1, \tag{50}$$

and

$$\Gamma_{\max} = \Gamma_\infty\left(1 + \frac{\gamma_\infty - \gamma_{\min}}{m_2}\right). \tag{51}$$

2.4. Initial boundary value problem and weak formulation

Balance equations and thermodynamic considerations give rise to the governing equations of the poromechanical problem, which in our case reads: Find the deformation mapping field $\boldsymbol{\varphi}$, the alveolar mapping field P_{alv} and the interfacial surfactant mass density field M_{surf} such that

$$\text{Div}\,(\boldsymbol{F}\boldsymbol{S}) + \boldsymbol{R}\boldsymbol{B} = \boldsymbol{0} \qquad \text{in } \Omega_R \times \mathbb{R}, \tag{52}$$

$$\frac{\partial \boldsymbol{\Phi}}{\partial t} + \text{Div}(\boldsymbol{Q}) = 0 \qquad \text{in } \Omega_R \times \mathbb{R}, \tag{53}$$

$$\frac{\partial M_{\text{surf}}}{\partial t} - \mathcal{F} = 0 \qquad \text{in } \Omega_R \times \mathbb{R}, \tag{54}$$

where the second Piola-Kirchhoff stress $\boldsymbol{S} = \boldsymbol{S}(\text{Grad}\,\boldsymbol{\varphi}, P_{\text{alv}}, M_{\text{surf}})$ is given by (42), the airflow follows the Darcy law (16), and the evolution law for the interfacial surfactant mass density field is given by (47). Eqs. (52) and (53) are complemented by boundary conditions

$$\boldsymbol{\varphi} = \bar{\boldsymbol{\varphi}} \qquad \text{on } \partial\Omega_{R_\varphi} \times \mathbb{R}, \tag{55}$$

$$(\boldsymbol{F}\boldsymbol{S}) \cdot \boldsymbol{N} = \bar{\boldsymbol{T}} \qquad \text{on } \partial\Omega_{R_T} \times \mathbb{R}, \tag{56}$$

$$P_{\text{alv}} = \bar{P} \qquad \text{on } \partial\Omega_{R_P} \times \mathbb{R}, \tag{57}$$

$$\boldsymbol{Q} \cdot \boldsymbol{N} = \bar{Q} \qquad \text{on } \partial\Omega_{R_Q} \times \mathbb{R}. \tag{58}$$

with $\boldsymbol{N}$ is the unitary vector normal to the reference configuration boundary $\partial\Omega_R$ and where we had assumed the partition (Li et al., 2004; Sun et al., 2013; Vuong et al., 2015)

$$\partial\Omega_{R_\varphi} \cup \partial\Omega_{R_T} = \partial\Omega_R \qquad \partial\Omega_{R_\varphi} \cap \partial\Omega_{R_T} = \emptyset, \tag{59}$$

$$\partial\Omega_{R_P} \cup \partial\Omega_{R_Q} = \partial\Omega_R \qquad \partial\Omega_{R_P} \cap \partial\Omega_{R_Q} = \emptyset, \tag{60}$$

with $\partial\Omega_{R_\varphi}$, $\partial\Omega_{R_T}$, $\partial\Omega_{R_P}$, and $\partial\Omega_{R_Q}$ the boundaries of prescribed deformation mapping, traction, alveolar pressure, and alveolar airflow, respectively. The formulation of our transient poromechanical problem is completed with the initial conditions for the primary variables $\boldsymbol{\varphi}$, P_{alv} and for the internal variable M_{surf}

$$\boldsymbol{\varphi} = \boldsymbol{\varphi}^0 \qquad \text{in } \Omega_R, \quad t = 0, \tag{61}$$

$$P_{\text{alv}} = P^0_{\text{alv}} \qquad \text{in } \Omega_R, \quad t = 0, \tag{62}$$

$$M_{\text{surf}} = M^0_{\text{surf}} \qquad \text{in } \Omega_R, \quad t = 0. \tag{63}$$

Following a standard finite-element procedure, we introduce the solution function spaces

$$\mathcal{S}_\varphi := \{\boldsymbol{\varphi} \mid \boldsymbol{\varphi} \in H^1(\Omega_R, \mathbb{R}^3);\ \boldsymbol{\varphi} = \bar{\boldsymbol{\varphi}} \ \text{ on } \partial\Omega_{R_\varphi}\}, \tag{64}$$

$$\mathcal{S}_P := \{P_{\text{alv}} \mid P_{\text{alv}} \in H^1(\Omega_R, \mathbb{R});\ P_{\text{alv}} = \bar{P} \text{ on } \partial\Omega_{R_P}\}, \tag{65}$$

$$\mathcal{S}_M := \{M_{\text{surf}} \mid M_{\text{surf}} \in L^2(\Omega_R, \mathbb{R})\} \tag{66}$$

and the associated test function spaces

$$\mathcal{V}_\varphi := \{\delta\boldsymbol{\varphi} \mid \delta\boldsymbol{\varphi} \in H^1(\Omega_R, \mathbb{R}^3);\ \delta\boldsymbol{\varphi} = \boldsymbol{0} \ \text{ on } \partial\Omega_{R_\varphi}\}, \tag{67}$$

$$\mathcal{V}_P := \{\delta P_{\text{alv}} \mid \delta P_{\text{alv}} \in H^1(\Omega_R, \mathbb{R});\ \delta P_{\text{alv}} = 0 \text{ on } \partial\Omega_{R_P}\}, \tag{68}$$

$$\mathcal{V}_M := \{\delta M_{\text{surf}} \mid \delta M_{\text{surf}} \in L^2(\Omega_R, \mathbb{R})\}. \tag{69}$$

Multiplying (52), (53) and (54) by their respective test functions, integrating into Ω_R, applying the integration by parts theorem when it is appropriate and using the boundary conditions (56), (58), we obtain the following weak statement

$$\int_{\Omega_R} \boldsymbol{F}\boldsymbol{S} : \text{Grad}\,\delta\boldsymbol{\varphi}\ dV - \int_{\Omega_R} \boldsymbol{R}\boldsymbol{B} \cdot \delta\boldsymbol{\varphi}\ dV - \int_{\partial\Omega_{R_T}} \bar{\boldsymbol{T}} \cdot \delta\boldsymbol{\varphi}\ dS = 0 \tag{70}$$

$$\int_{\Omega_R} \frac{\partial \boldsymbol{\Phi}}{\partial t}\ \delta P_{\text{alv}}\ dV - \int_{\Omega_R} \boldsymbol{Q} \cdot \text{Grad}\,\delta P_{\text{alv}}\ dV + \int_{\partial\Omega_{R_Q}} \bar{Q}\ \delta P_{\text{alv}}\ dS = 0 \tag{71}$$

$$\int_{\Omega_R} \left\{ \frac{\partial M_{\text{surf}}}{\partial t} - \mathcal{F} \right\} \cdot \delta M_{\text{surf}}\ dV = 0 \tag{72}$$

for all $(\delta\boldsymbol{\varphi}, \delta P_{\text{alv}}, \delta M_{\text{surf}}) \in \mathcal{V}_\varphi \times \mathcal{V}_P \times \mathcal{V}_M$. Eq. (72) was solved pointwise since gradients of M_{surf} are not involved (Hurtado et al., 2017a; Hurtado and Zavala, 2021). Temporal discretization of the weak formulation was carried out using a backward-Euler time integration scheme. We implement the temporally discretized problem in the finite element FEniCS library (Logg et al., 2012).

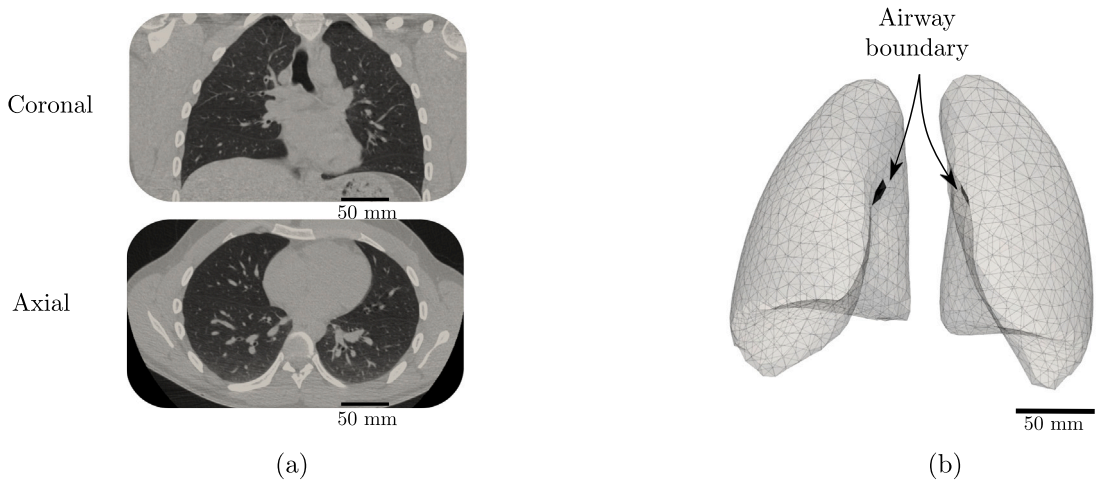

Fig. 2. Construction of an anatomical finite-element model of the lungs: (a) Coronal and axial slices of computed-tomography image of a normal human lung at end of expiration, assumed as the reference configuration. (b) Tetrahedral mesh considered in finite element simulations. The airway boundaries are shown in black.

Table 1
Model parameters considered in numerical simulations. Note that for the purely elastic lung simulations, only a, b, c and κ/η are necessary. *Values were computed from the alveolar dimensions given in the reference.

Parameter	Value	Units	Reference
Γ_∞	$3.0 \cdot 10^{-9}$	g/mm^2	Morris et al. (2001)
$\gamma_{\min}$	0	N/mm	Pattle (1955)
γ_0	$70 \cdot 10^{-6}$	N/mm	Otis et al. (1994)
m_1	$47.8 \cdot 10^{-6}$	N/mm	Otis et al. (1994)
m_2	$140 \cdot 10^{-6}$	N/mm	Otis et al. (1994), Morris et al. (2001)
k_1	$1.6 \cdot 10^8$	mm^3/(g s)	Otis et al. (1994), Denny and Schroter (2000)
k_2	0.016	1/s	Otis et al. (1994), Denny and Schroter (2000)
C	$7.3 \cdot 10^{-9}$	g/mm^3	Otis et al. (1994), Denny and Schroter (2000)
R_{RE}	0.11	mm	Jbaily et al. (2020)*
Φ_R	0.74	–	Jbaily et al. (2020)*
a	0.433	–	Tawhai et al. (2009)
b	−0.61	–	Tawhai et al. (2009)
c	2.5	kPa	Tawhai et al. (2009)
κ/η	10^4	mm^2/(kPa s)	Berger et al. (2016), Avilés-Rojas and Hurtado (2022)

3. Numerical simulations

3.1. Model setup and post-processing

The lung domain was segmented from a computed tomography image taken from a healthy volunteer under resting conditions (Hurtado et al., 2017b), see Fig. 2(a) for coronal and axial slices. The computational tetrahedral mesh was generated using the CGAL library (The CGAL Project, 2021). We considered this mesh to be the reference stress-free configuration Ω_R, see Fig. 2(b). The lung surface was partitioned into the airway boundaries ($\partial\Omega_{R_{aw}}$) and the visceral pleura surface ($\partial\Omega_{R_{pl}}$). The visceral pleura surface was assumed isolated, i.e., no-flux boundary conditions for the flow field. The airway boundary allowed airflow, either by prescribing pressures or flow (Avilés-Rojas and Hurtado, 2022). Considering that the focus of this work was to model and validate the effect of surface tension on lung mechanics, our simulations considered an excised lung, and therefore the lung surface was free to displace without any mechanical restraint. This condition is consistent with the *in-vitro* experimental setup of the supersyringe method (Mead et al., 1957), which we explain below. Accordingly, the visceral pleura surface was assumed to have zero-traction boundary conditions. Null displacements were prescribed over the airway boundary to prevent rigid-body modes. Throughout our experiments, we assumed that the reference and initial configuration match, which implies $\boldsymbol{\varphi}^0 = \mathbf{0}$, $P^0_{\text{alv}} = 0$ and $M^0_{\text{surf}} = M^R_{\text{surf}}$. In particular, we set $M^R_{\text{surf}} = \Gamma_{\max} A^0(\boldsymbol{X})$, with A^0 the initial alveolar area density field computed directly from the reference alveolar geometry, and $\Gamma_{\max}$ the value of the interfacial surfactant concentration such that the minimum surface tension was zero. The values for $\Gamma_{\max}$ and other parameters assumed for a normal lung, also called (hyper) elastic with surface tension (EL+ST) lung, are shown in Table 1 along with references where these values were taken from. In addition to modeling a normal lung, we consider the case in which the effects of surface tension were deactivated ($\gamma = 0$), which we refer to as purely elastic (EL) lung.

A standard approach to studying lung mechanics is the construction of quasi-static pressure–volume curves from the supersyringe experiment (Mergoni et al., 1997). This method includes inflation and deflation stages, requiring the lungs to be connected to a large (super) syringe. During the inflation stage, the syringe plunger is moved in regular steps, allowing a small volume of air, typically about 100 ml, to be delivered to the lungs at each step. A 2 or 3-second pause is performed between two successive steps to reach the quasi-static state. Deflation is carried out similarly to the inflation stage once a predefined air volume or airway pressure is reached. Volume and airway pressure data are recorded during the experiment (Harris, 2005). In this work, we used the proposed lung model to construct P–V curves by simulating a supersyringe experiment. During the inflation stage, a total air volume V_T was supplied step by step in N_s regular steps. Each step was divided into two phases: a flow phase, with duration T_f and a pause phase of duration T_p. During the flow phase, air was supplied by imposing a constant flow $\bar{Q} = V_s/(A_\mathrm{aw} T_\mathrm{f})$ where $V_s = V_T/N_s$ is the volume supply in each step and A_aw is the area of the airways boundary computed as the surface integral over this boundary. Then, flow was set to zero throughout the pause phase. After reaching the target volume, the deflation process was carried out using an analogous procedure, expelling the air step by step. During the entire experiment, we computed the temporal evolution of the volume supplied by the syringe, also called lung volume (V), the average airway pressure (P), and the average surface tension (γ), defined as

$$\mathrm{V}(t) := \int_{\Omega_R} (J-1)\, dV, \quad \mathrm{P}(t) := \frac{1}{A_\mathrm{aw}} \int_{\partial\Omega_{R_\mathrm{aw}}} P_\mathrm{alv}\, dS, \quad \gamma(t) := \frac{1}{V_R} \int_{\Omega_R} \gamma\, dV \tag{73}$$

where V_R is the reference lung volume obtained as $V_R = \int_{\Omega_R} dV$. From these data, the quasi-static pressure–volume and surface tension-volume (γ-V) curves were constructed connecting the last point of each step. We set $T_\mathrm{f} = 0.3$ s, $T_\mathrm{p} = 2.0$ s and $V_s = 0.1$ L in our supersyringe simulations. Three different volume excursions for the elastic with surface tension lung were simulated: a baseline volume of $V_T = 1.5$ L, a low volume of $V_T = 0.5$ L, and a high volume of $V_T = 2.5$ L. Quasi-static curves for the purely elastic lung were also constructed for the baseline volume.

Volume-controlled mechanical ventilation (VCV) simulations were also performed for the elastic with surface tension and the purely elastic lungs; we refer the reader to Avilés-Rojas and Hurtado (2022) for further details of the simulation protocol. During the first phase of this ventilation mode, i.e., inspiration phase, a tidal volume V_tidal was supplied by prescribing a constant airflow $\bar{Q} = V_\mathrm{tidal}/(A_\mathrm{aw} T_\mathrm{insp})$ on the airway boundary, with T_insp the duration of the inspiratory phase. After this, a pause phase was simulated, during which a null flow was prescribed on the airway boundaries. Next, the expiration was carried out by setting the airway pressure equal to zero. In addition to the lung volume, airway pressure, and surface tension given by (73), the flow of air was computed as $\dot{V}(t) = \partial V(t)/\partial t$. For our VCV experiments, we considered an inspiratory phase of 1.5 s in which a tidal volume of 0.5 L was supplied, followed by 0.75 s of pause and an expiratory phase of 4.5 s.

3.2. Results

Fig. 3 shows the temporal evolution of the lung volume, airway pressure, and average surface tension for the normal (elastic with surface tension) lung and the deactivated surface-tension (purely elastic) lung cases. The evolution of pressure and surface tension for the normal lung strongly differed between the inflation and deflation branches. For example, during inflation, the surfactant behavior changed from an insoluble regime to a regime governed by Langmuir kinetics at $t = 9.8$ s, in which the surface tension tended to equilibrium, remaining in that regime until the end of the inflation phase. In contrast, during the deflation phase, this regime was quickly abandoned, passing to an insoluble state and finally producing squeeze-out phenomena when the minimum surface tension was reached during the dynamic compression of the syringe phase.

The quasi-static pressure–volume curves constructed from the volume and pressure time series are reported in Fig. 4(a). The inflation and deflation limbs for the purely elastic lung case coincide and are nearly linear in the range of volume and pressure considered. In large contrast, in the elastic with surface tension lung simulation, the inflation and deflation limbs considerably differ, resulting in a markedly hysteretic behavior. Changes in the slope of P–V curves, also known as lung compliance, were observed during inflation and deflation. Following the notation given in Takeuchi et al. (2001), the different slopes in the P–V curve are denoted as $\mathrm{C_{start}}$ (starting compliance), $\mathrm{C_{inf}}$ (inflation compliance), $\mathrm{C_{top}}$ (top compliance), $\mathrm{C_{def}}$ (deflation compliance), and the compliance transitioned points as LIP (lower inflection point) and PMC (point of maximum curvature). Fig. 4(b) reports the surface tension-volume curve. For the elastic with surface tension lung, the γ-V curve displayed a non-linear behavior.

To study the spatial distribution of volumetric changes and the gas fraction, we report the Jacobian and the Eulerian porosity fields in the elastic with surface tension and purely elastic lung simulations for airway pressures of 2 and 5 cm $\mathrm{H_2O}$ during inflation and deflation, see Figs. 5(a) and (b). Fig. 5 also reports the tissue hydrostatic stress field, defined as $\sigma^\mathrm{hyd}_\mathrm{tissue} = (1/3)\mathrm{tr}\left(\boldsymbol{\sigma}_\mathrm{tissue}\right)$ with $\boldsymbol{\sigma}_\mathrm{tissue} = \boldsymbol{J}^{-1}\boldsymbol{F}\left(\partial\Psi^\mathrm{el}/\partial\boldsymbol{E}\right)\boldsymbol{F}^T$. The Jacobian, Eulerian porosity, and hydrostatic stress fields for the elastic with surface tension lung resulted in lower values during inflation than deflation. For example, for an airway pressure of 5 cm $\mathrm{H_2O}$, Eulerian porosity reached a maximum of 0.77 during inflation, while this value increased to 0.81 during deflation. In contrast, no differences were observed during inflation and deflation in the purely elastic lung simulation. The spatial distribution of Jacobian, Eulerian porosity, and tissue hydrostatic stress fields for an axial slice and the lung surface are included in the supplementary material.

Fig. 6(a) shows the pressure–volume curves for the low, baseline, and high volume cases for the elastic with surface tension lung. The high-volume case displayed larger hysteresis compared to other cases, represented by the area enclosed by inflation and deflation limbs. Interestingly, the change in compliance from $\mathrm{C_{start}}$ to $\mathrm{C_{inf}}$ is similar for the baseline and high volume simulations. In contrast, changes in hysteresis and slope in the low-volume case were negligible. Fig. 6(b) shows the surface tension-volume curve for the three volume cases. While the surface tension for the low-volume simulation seems to remain under an insoluble regime

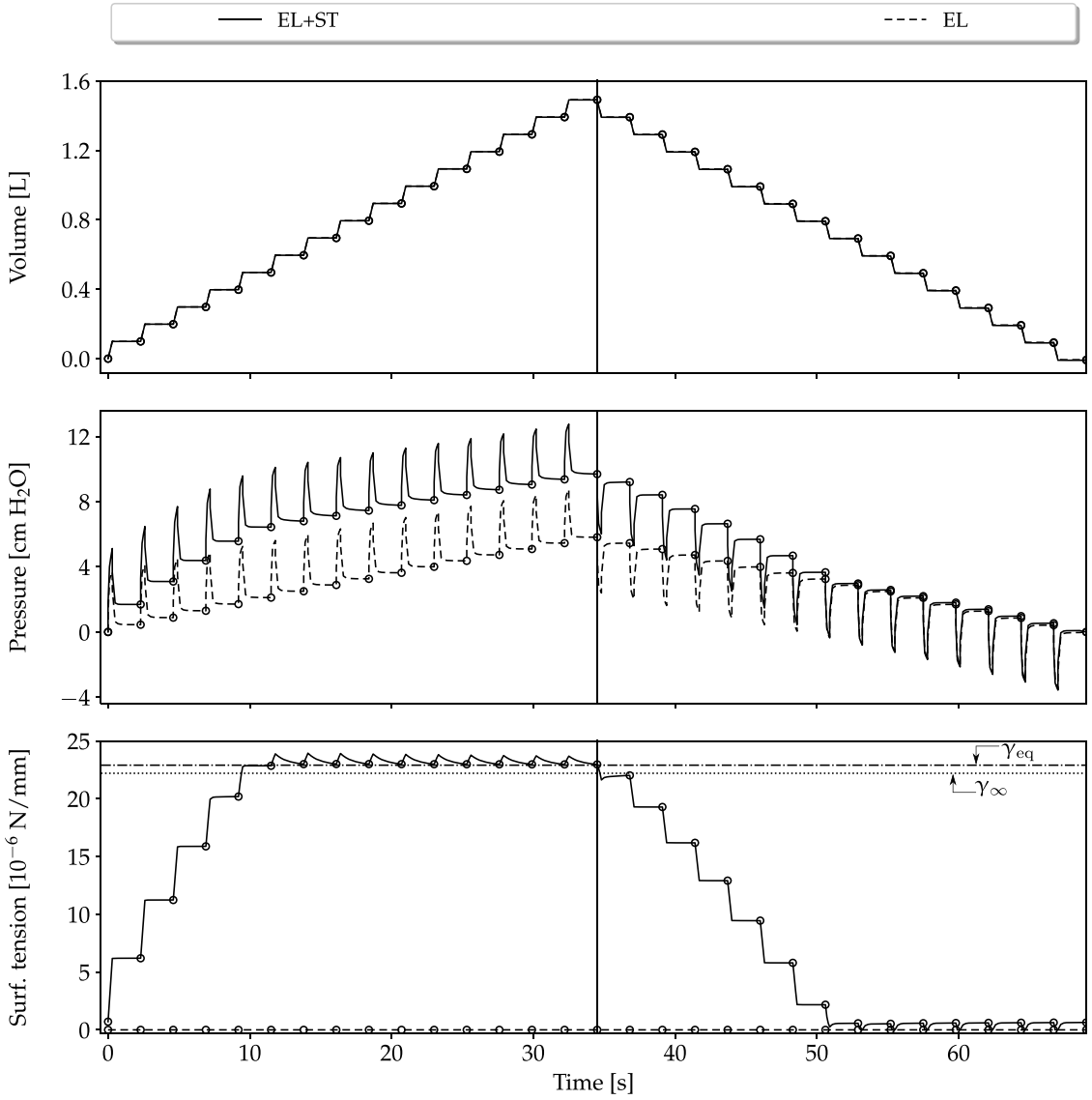

Fig. 3. Simulation of the supersyringe method for elastic tissue model with surface tension (EL+ST) and purely elastic tissue model (EL). Temporal evolution of lung volume, airway pressure, and surface tension is shown for both cases. Black dots indicate the steady-state time instants considered in the construction of quasi-static pressure–volume curves. We note that γ_{eq} is the equilibrium surface tension, and γ_{∞} is the surface tension corresponding to the threshold between the insoluble and Langmuir regimes.

($\gamma < \gamma_{\infty}$), the other cases exceed the value of γ_{∞}, moving to a Langmuir regime, in which the surface tension tends to equilibrium γ_{eq}.

Fig. 7(a) shows the airway pressure, flow, volume, and surface tension signals calculated for the VCV simulations. In this experiment, volume and flow signals during the inspiratory phase are the same for the elastic with surface tension and the purely elastic lung simulations. Maximum inspiratory pressure was higher in the elastic with surface tension lung than in the purely elastic lung. We also observed marked differences in flow and volume waveforms during the expiratory phase. Figs. 7(b) and 7(c) show the corresponding dynamic pressure–volume curves and the dynamic surface tension-volume curves, respectively. Both dynamic pressure–volume curves exhibit hysteresis, even though the dynamic surface tension-volume curves do not.

4. Discussion

In this work, we introduce a continuum poromechanical model of lung mechanics that incorporates the effect of surfactant dynamics and the resulting alveolar surface tension on the tissue and organ response. Previous continuum formulations of lung mechanics only considered the hyperelastic tissue response and its interaction with gas viscous flow, resulting in standard poroelastic

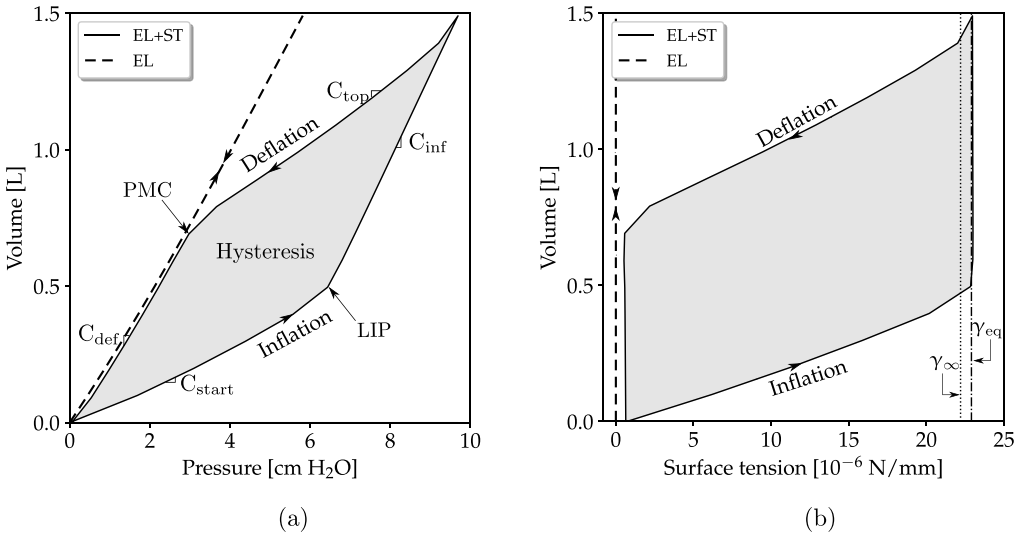

Fig. 4. Quasi-static pressure–volume curves for elastic with surface tension (EL+ST) and purely elastic (EL) lungs: (a) pressure–volume curves and (b) surface tension-volume curves. Slopes in the P–V inflation limb are indicated as C_{start} and C_{inf}, while during deflation limb as C_{top} and C_{def}. The lower inflection point (LIP) and point of maximum curvature (PMC) correspond to breakpoints in the P–V curve where slope abruptly changes during inflation and deflation, respectively. The shaded area in the P–V curve indicates the energy dissipation or quasi-static hysteresis due to the surface tension effect of pulmonary surfactant. Note that γ_{eq} is the equilibrium surface tension, and γ_{∞} is the surface tension corresponding to the threshold between the insoluble and Langmuir regimes.

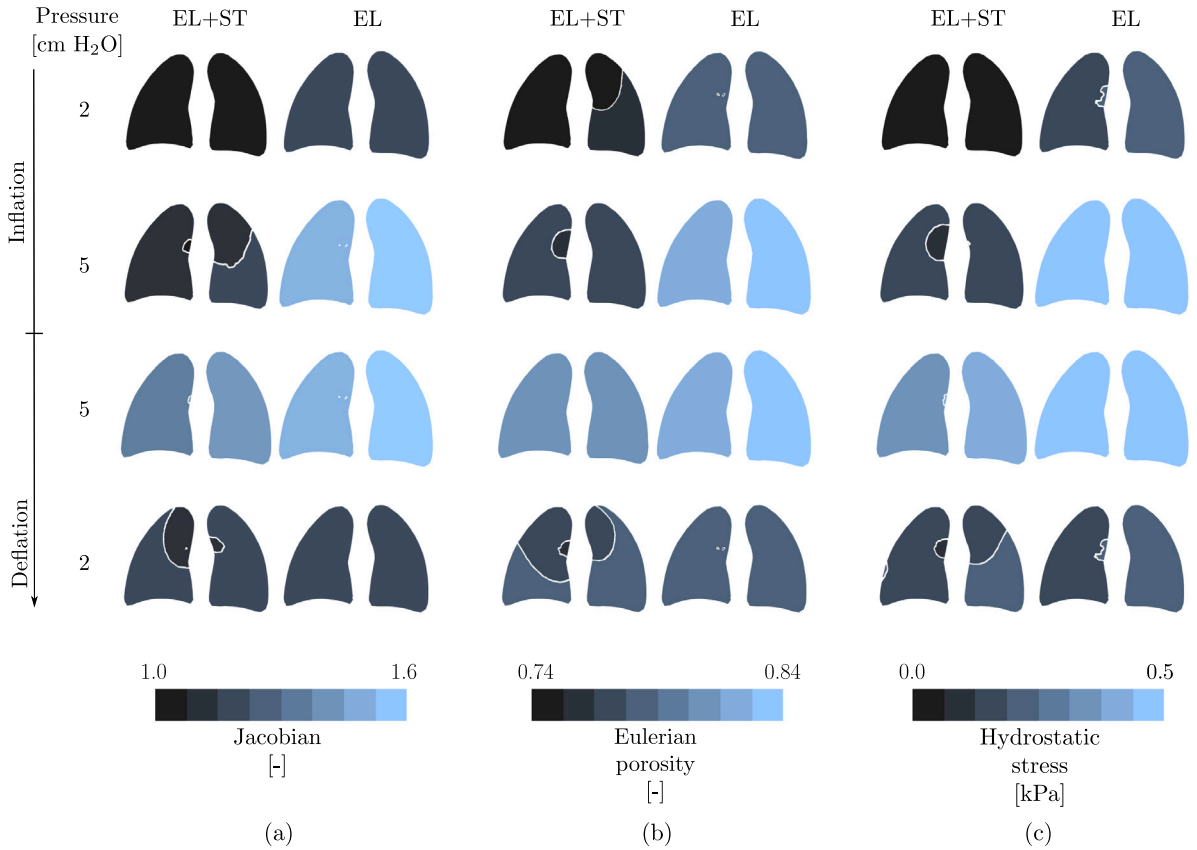

Fig. 5. Three-dimensional fields at different pressure levels during the supersyringe method simulation for elastic with surface tension (EL+ST) and purely elastic (EL) lungs: (a) Jacobian volume-change field, (b) Eulerian porosity field, (c) tissue hydrostatic stress field.

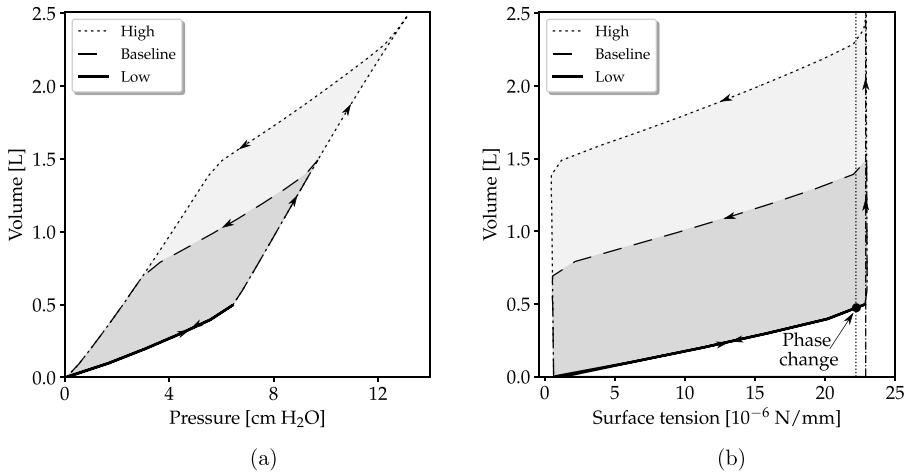

Fig. 6. Influence of total excursion volume on quasi-static lung response: (a) pressure–volume curves and (b) surface tension-volume curves. No hysteresis is observed for the low-volume case. A black dot on the $\gamma - V$ curve indicates when, on average, the behavior of the pulmonary surfactant changes from an insoluble regime to one governed by Langmuir kinetics. The inflation and deflation limbs for the low-volume case coincide.

models (Berger et al., 2016; Patte et al., 2022; Avilés-Rojas and Hurtado, 2022; Hurtado et al., 2023). To the best of our knowledge, our work constitutes the first attempt to directly address interfacial phenomena resulting from the thin liquid layer surrounding the alveolar tissue and in contact with the air in a continuum formulation, whose impact on pulmonary function is crucial. Due to the scale differences between surfactant and whole organ, surfactant activity was naturally considered in a continuous framework using an internal variables theory approach. This approach allows us to track the surfactant mass in the interface and the consequent transient behavior of surface tension during multiple-step experiments as the supersyringe method; see the surface tension evolution in Fig. 3. Further, via a standard Coleman–Noll procedure and taking the mass of the surfactant as a new state variable, we obtain an expression of Clausius–Duhem inequality similar to the usual one for poroelastic media with incompressible solid matrix (Coussy, 2004), plus two new terms: a term opposite to pore pressure that takes into account surface tension; and a dissipative term due to the adsorption–desorption of the surfactant, see Eq. (33). This expression results in a stress tensor formulation that integrates tissue elasticity and surface tension, the main mechanisms of lung recoil (Bachofen et al., 1970; Wilson, 1982). Further, the surface tension-related term is essentially similar to the classical Young–Laplace equation but modulated by a geometric factor representing the porous nature of alveoli, see (42). Based on this result, we anticipate that the zero-thickness bubble alveolar model traditionally used (Steimle et al., 2011) could be suitable for highly porous alveolar tissue (high value of Φ_R). However, it may not be suitable to take into account the effect of surface tension in lungs with low porosity (low gas fraction), as collapsing pressure P_γ increases when the Lagrangian porosity Φ decreases (Nikooee et al., 2013).

The pressure–volume curve is a gold-standard tool to characterize the mechanical properties of the lung, providing critical information to manage the treatment of patients with respiratory distress during mechanical ventilation treatment (Harris, 2005; Albaiceta et al., 2008). Remarkably, our computational model allows the construction of these curves, recovering many features of representative P–V curves observed in medical research and clinical practice (Takeuchi et al., 2001; Quiros et al., 2022). Notably, our results suggest that the P–V inflation and deflation limbs are strongly influenced by the shape of the surface tension-volume curve ($\gamma - V$), see in Fig. 4(b). For example, during the loading phase (inflation), surface tension increases with volume, in a similar way to the pressure, until the equilibrium surface tension (γ_{eq}) is reached. In particular, we note that the volume when the surface tension reaches the equilibrium coincides with the improvement in compliance during inflation. We highlight that in clinical practice, this transition from low to high compliance is known as the lower inflection point (LIP) and is used as a guide to set the optimal value of the positive end-expiratory pressure (PEEP) in mechanically ventilated patients because it has been historically related to the recruitment of alveolar units (Suter et al., 1975; Jonson and Svantesson, 1999; Harris, 2005). Interestingly, our predicted LIP is mainly attributed to the dynamics of the surfactant, which transitions from an initially compressed state of very low compressibility (change in surface area per change in surface tension) to a regime with high surface compressibility (Smith and Stamenovic, 1986). We remark that our results are consistent with the experimental results of Smith and Stamenovic (1986) (see, for example, Figure 6 of that reference), which show that the shape of P–V curves is directly determined by the molecular properties of the surfactant film relating to the non-equilibrium behavior and adsorption–desorption regime. Our results capture the critical role of surface tension in establishing trend changes and breakpoints in P–V curves, as supported by previous contributions in the literature (Hubmayr, 2002), which along with alveolar recruitment, constitutes one of the main drivers of lung compliance (Jonson and Svantesson, 1999).

One of the most remarkable features of our model is its ability to capture dissipative phenomena due to interfacial dynamics such as the quasi-static hysteresis, a common feature observed in quasi-static pressure–volume curves of healthy and diseased lungs (Gibson and Pride, 1976; Matamis et al., 1984), see the P–V hysteretic loop shown in Fig. 4(a) for the elastic with surface tension lung. In effect, for the same change in volume, higher pressures are necessary during inflation than deflation, which implies

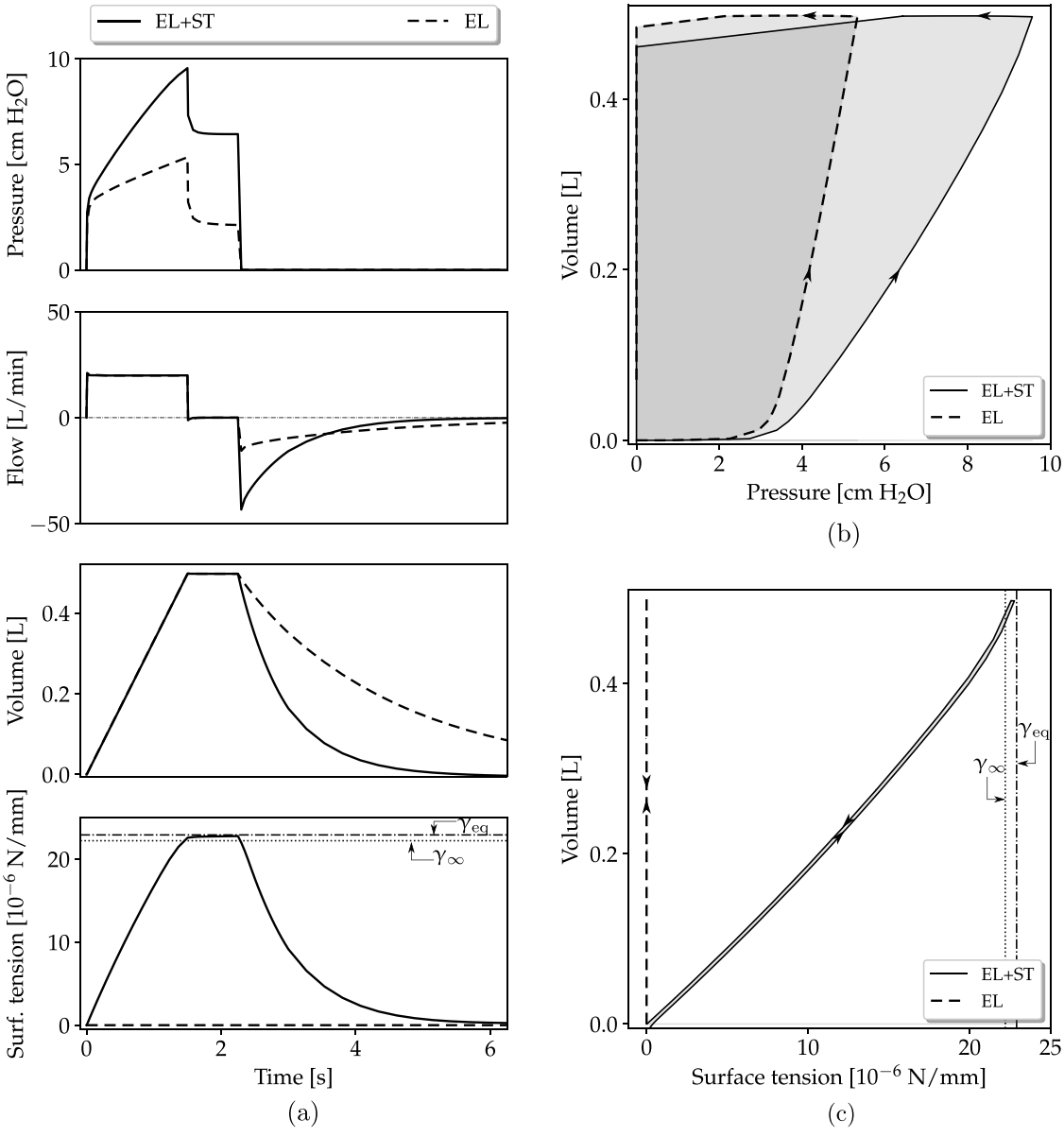

Fig. 7. Volume-controlled mechanical ventilation simulations of elastic with surface tension (EL+ST) and purely elastic (EL) lungs: (a) airway pressure, flow, lung volume, and surface tension signals, (b) dynamic pressure–volume curve, and (c) dynamic surface tension-volume curve. Note that γ_{eq} is the equilibrium surface tension, and γ_{∞} is the surface tension corresponding to the threshold between the insoluble and Langmuir regimes.

that a greater amount of mechanical work must be done to open the lung than to close it (Hess, 2014). This quasi-static hysteresis is consistent with experimental setups on excised air-filled lungs (Mead et al., 1957) and can be attributed to the asymmetry of lung surfactant film behavior during inflation and deflation (Suki et al., 2011; Goerke, 1998), as Fig. 3 shows. Consequently, different pressures are needed for inflation and deflation, and the energy applied during inflation is not fully recovered in the deflation process (Escolar and Escolar, 2004). Our spatial distribution field predictions also capture the hysteresis-related differences between inflation and deflation stages for the elastic with surface tension lung; see Fig. 5. In particular, for the same pressure level, the Jacobian distributions suggest that alveolar units are more open during deflation than inflation, which implies a higher gas fraction in the deflation stage, as the Eulerian porosity field shows. As we expected, in the purely elastic lung there are no differences between inflation and deflation limbs for the same pressure level, that is in line with *in-vitro* pressure–volume curves on saline-filled lungs in which surface tension and hysteresis are negligible. Furthermore, we note that the absence of collapsing pressure due to surface tension results in larger volumetric changes and tissue hydrostatic stresses than in the elastic with surface tension lung case. We remark that quasi-static hysteresis of the whole lung has been previously predicted by discrete models, as proposed by Roth et al. (2017). However, in that model, alveolar ducts were modeled using a four-element Maxwell model (Ismail et al.,

2013) with viscoelastic parameters calibrated from previous numerical P–V curves (Denny and Schroter, 2000), not allowing a direct relationship of the lung mechanics with surfactant properties. Recently, a whole lung acinar units computational model that incorporated the dynamic surfactant physicochemical behavior in the air–liquid interface and the resulting (Laplace) collapsing pressure was proposed (Ma et al., 2020, 2023). The authors report dynamic curves for low tidal volume breathing but not the quasi-static pressure–volume curves that are usually used to quantify the surfactant contribution to hysteresis. In contrast, here we show that our poromechanical framework can represent the quasi-static hysteretical lung behavior, which is directly influenced by the dynamics of surfactant at the alveolar level.

The influence of volume excursion in the shape of pressure–volume curves was also analyzed; see Fig. 6. We note that, while for long excursions, it is possible to identify the lower inflection point on the inflation limb and the point of maximum curvature on the deflation limb, which indicate the changes in compliance during inflation and deflation, respectively, no marked compliance changes are observed for small volumes. Further, we note that the LIP value and the start compliance C_{start} for the medium and longest volumes are similar. These observations suggest that, while the LIP depends on the total volume and does not exist for low volumes, C_{start} and the LIP value (if any) are not influenced by the total volume. Interestingly, the PMC is strongly affected by volume, having a high-pressure value for longer excursions. Notably, many of our volume-dependent predictions are in line with the observations from experimental measurements performed by Takeuchi et al. (2001). Another notable result of our model is the effect of the volume excursion on the difference between the inspiratory and expiratory limbs, which results in larger hysteresis for larger volumes, being negligible for small volumes. We note that this fact has been previously reported for quasi-static P–V curves for human lungs, which suggest that under small deformations, the lung behavior is similar to an ideal elastic (reversible) medium and that non-reversibility phenomena are produced during deep volume cycles, resulting in the lung hysterical behavior (Mead et al., 1957). Remarkably, our thermodynamic framework suggests that the value of γ_∞, that is, the surface tension that triggers the surfactant phase-change towards the Langmuir regime, corresponds to a threshold that separates a purely elastic domain and a dissipative one. In this sense, it plays a similar role to the yield stress observed in plasticity theory. In effect, surfactant-related dissipated energy would only exist if the non-equilibrium (Langmuir) regime is achieved, leaving an almost elastic behavior for volume levels that do not experience the phase change from insoluble to Langmuir regime.

The applicability of the proposed framework to clinical situations was studied by means of simulating mechanical ventilation protocols typically used in patients with lung failure. We observed that our lung simulations were able to predict the evolution of key respiratory signals such as airway pressure, lung flow, and lung volume, see Fig. 7(a), recovering waveforms readily observed in the clinical practice. For example, the airway pressure increases throughout inspiration due to the square wave of prescribed flow and is then reduced during the pause phase until reaching a plateau pressure, which tends to a steady state. In addition, the negative flow peak and its exponential decay during expiration, usually observed in patients under mechanical ventilation (Ball et al., 2015), also is recovered. Our model shows that the surface tension seems to have an essential influence on the magnitude and shape of these physiological signals. In particular, for the same change in lung volume, the peak inspiratory and plateau pressure are higher for the elastic with surface tension (normal) case. The higher elastic recoil pressure in normal lungs can explain these larger values. Indeed, the elastic recoil of the purely elastic lung is completely explained by the lung tissue elasticity and is only a fraction of the recoil of the normal lung that also considers the collapsing pressure due to surface tension P_γ (Kylstra and Schoenfisch, 1972). Consequently, a higher magnitude of the maximum expiratory flow and a lower exponential decay time constant are predicted when surface tension is included. Interestingly, even though the surface tension is neglected in the purely elastic situation, a hysteretical loop in the dynamic pressure–volume curve is produced. We attribute this dissipative behavior to the airflow in the lung parenchyma; see Eq. (14). A further qualitative comparison between the areas enclosed by the dynamic pressure–volume curves in Fig. 7(b) shows that most of the dynamic hysteresis arises due to flow resistance rather than surface tension. In fact, the contribution of surfactant dynamics to lung hysteresis during transient breathing cycles with low tidal volumes is negligible (Suki et al., 2011; Schürch et al., 1992).

Some similarities and important differences with models used in applications in areas other than lung biomechanics are presented in our framework. In particular, the stress constitutive relationship (42), see also Eq. (34), corresponds to the standard expression in standard Biot (1941) poromechanics plus an additional term associated with the collapse pressure due to surface tension, which in essence represents a capillary force similar to that found in the model of Bishop (1959) for representing partially saturated soils. In that model, the capillary force term is usually considered to be a constitutive function of the volume fraction rather than an explicit function of the interfacial areas (see, for instance, Laloui et al. (2003), Coussy (2007), Alonso et al. (2010)). In contrast, in our model, the capillary-like term, i.e., the term containing P_γ, is defined as a function of the air–liquid interface area, highlighting the relevance of interfacial phenomena in alveolar mechanics. This approach is based on the assumption that the volumetric contribution of the liquid lining layer is negligible compared to the interfacial forces and that there is no direct contact between tissue and air, reasonable conditions in healthy lung parenchyma (Knudsen and Ochs, 2018). In addition, Eq. (43), derived assuming a spherical shell geometry for alveolus, also introduces a novel expression for the capillary-like term that allows capturing geometric effects of lung microstructure within a thermodynamically consistent framework. Although the geometric assumption of a spherical cavity is widely employed in respiratory mechanics, it is important to recognize that there is histological and theoretical evidence to suggest that an alveolus is best represented by a polyhedron and, in particular, by a tetrakaidecahedron rather than perfectly rounded structures (Fung, 1988). Further, lung physiology literature also suggests that the alveolar geometry is affected by lung volume changes varying from a polyhedral to a more spherical shape (Gil et al., 1979). Another noteworthy contribution of this work is the fact that the surfactant dynamics represented through an evolution law is integrated in a continuum framework, resulting in a model in which the surface tension (and hence the stress tensor) is dependent on the amount of interfacial surfactant. We note that surface tension that depends on the concentration of the adsorbed compound has been integrated, for example, in modeling the

phenomenon of adsorption-induced swelling of carbon dioxide-infiltrated coals (Vandamme et al., 2010; Zhang, 2018). However, while in those studies, the adsorbed compound corresponds to the fluid phase, in our study, adsorption is considered an internal process within the porous medium matrix.

This work corresponds to one of the first attempts to incorporate surface tension into a continuous lung model, offering many opportunities for improvement. First, our simulations assumed an unstressed reference configuration based on the geometry of the lung at the end of expiration. This assumptions is limited in that prestresses are present during resting conditions due to effect of pleural pressure acting over the lung surface. Some works in the literature have addressed this limitation by estimating the unloaded configuration using fixed-point techniques (Patte et al., 2022; Berger et al., 2016). However, the experimental validation of methods for the determination of prestress fields remains an open problem. Second, despite the fact that we have captured the inelastic effects linked to surfactant-dependent surface tension, the viscoelastic response of alveolar tissue and the recruitment/derecruitment of the airway and alveolar units has not been considered. While hysteresis of surfactant is negligible for normal tidal breathing, tissue viscoelasticity could result in hysteretical loops during these low-volume regimes (Schürch et al., 1992; Suki et al., 2011), which is not reflected in our simulations. We note that tissue viscoelasticity could be incorporated in our continuum model using finite-deformation viscoelastic material models, which adds to a non-equilibrium stress term to the expression of the second Piola Kirchoff tensor (Birzle and Wall, 2019; Holzapfel, 2002). The recruitment/derecruitment mechanism has also been related to pulmonary hysteresis (Escolar and Escolar, 2004). While theoretical models that capture the time-dependent lung mechanical response due to gradual recruitment/recruitment have been proposed (Bates and Irvin, 2002), continuum models that account for this phenomenon still need to be developed. Third, conducting and respiratory airways that compose the complex airway tree structure inside the lung have not been explicitly modeled. Instead, the right and left primary bronchial tubes have been considered a boundary of the domain, allowing air to enter or exit, while the rest of the airways are assumed to be part of the porous medium. As a consequence, lung ventilation is mainly influenced by the conductivity of the porous medium. A simple approach to represent the interaction between the airway tree and lung parenchyma is to couple the lung continuum model with a dyadic resistive pipe network that follows the anatomical airway geometry (Berger et al., 2016; Pozin et al., 2017). Fourth, in this study, we considered excised lung without mechanical restrictions on its surface. While this approach is adequate to estimate the lung pressure–volume relationship, the mechanical constraints of the rib cage, diaphragm, and mediastinum should be assessed to simulate mechanical ventilation more physiologically. In this context, the mechanical interaction between the lung surface and its surrounding structures can be modeled through elastic spring elements or by prescribing a frictionless contact boundary condition (Patte et al., 2022). Finally, applying our model to lung diseases in which pulmonary surfactant has a critical pathophysiological role remains a future challenge. Future contributions should be analyzing the effect of an impaired and decreased pulmonary surfactant production in the lung response, which is especially critical in patients with acute respiratory distress syndrome connected to mechanical ventilation, who could present abnormally high levels of surface tension and, consequently, collapsed lung regions and highly heterogeneous regional ventilation (Albert, 2012; Levy, 2002; Retamal et al., 2018).

CRediT authorship contribution statement

Nibaldo Avilés-Rojas: Writing – original draft, Visualization, Validation, Software, Methodology, Investigation, Formal analysis, Conceptualization. **Daniel E. Hurtado:** Writing – review & editing, Writing – original draft, Visualization, Supervision, Resources, Project administration, Investigation, Funding acquisition, Formal analysis, Conceptualization.

Declaration of competing interest

The authors declare that they have no known competing financial interests or personal relationships that could have appeared to influence the work reported in this paper.

Acknowledgments

This work was funded by the Agencia Nacional de Invetigación y Desarrollo (ANID) Chile through the grant FONDECYT Regular # 1220465. NA-R acknowledges the support of the graduate fellowship ANID Beca Doctorado Nacional 21212320.

Appendix A. Supplementary data

Supplementary material related to this article can be found online at https://doi.org/10.1016/j.jmps.2025.106174.

Data availability

Data will be made available on request.

References

Albaiceta, G.M., Blanch, L., Lucangelo, U., 2008. Static pressure–volume curves of the respiratory system: were they just a passing fad? Curr. Opin. Crit. Care 14 (1), 80–86.

Albert, R.K., 2012. The role of ventilation-induced surfactant dysfunction and atelectasis in causing acute respiratory distress syndrome. Am. J. Respir. Crit. Care Med. 185 (7), 702–708.

Alonso, E.E., Pereira, J.M., Vaunat, J., Olivella, S., 2010. A microstructurally based effective stress for unsaturated soils. Géotechnique 60 (12), 913–925.

Avery, M.E., Mead, J., 1959. Surface properties in relation to atelectasis and hyaline membrane disease. AMA J. Dis. Child. 97 (5_PART_I), 517–523.

Avilés-Rojas, N., Hurtado, D.E., 2022. Whole-lung finite-element models for mechanical ventilation and respiratory research applications. Front. Physiol. 2060.

Bachofen, H., Hildebrandt, J., Bachofen, M., 1970. Pressure-volume curves of air-and liquid-filled excised lungs-surface tension in situ. J. Appl. Physiol. 29 (4), 422–431.

Ball, L., Dameri, M., Pelosi, P., 2015. Modes of mechanical ventilation for the operating room. Best Pr. Res. Clin. Anaesthesiol. 29 (3), 285–299.

Bates, J.H., 2009. Lung Mechanics. An Inverse Modeling Approach. p. 218.

Bates, J.H., Irvin, C.G., 2002. Time dependence of recruitment and derecruitment in the lung: a theoretical model. J. Appl. Physiol. 93 (2), 705–713.

Ben-Tal, A., 2006. Simplified models for gas exchange in the human lungs. J. Theoret. Biol. 238 (2), 474–495.

Berger, L., Bordas, R., Burrowes, K., Grau, V., Tavener, S., Kay, D., 2016. A poroelastic model coupled to a fluid network with applications in lung modelling. Int. J. Numer. Methods Biomed. Eng. 32 (1).

Biot, M.A., 1941. General theory of three-dimensional consolidation. J. Appl. Phys. 12 (2), 155–164.

Birzle, A.M., Wall, W.A., 2019. A viscoelastic nonlinear compressible material model of lung parenchyma–experiments and numerical identification. J. Mech. Behav. Biomed. Mater. 94, 164–175.

Bishop, A.W., 1959. The principle of effective stress. Tek. Ukebl. 39, 859–863.

Butt, H.J., Graf, K., Kappl, M., 2023. Physics and Chemistry of Interfaces. John Wiley & Sons.

Chiew, Y.S., Tan, C.P., Chase, J.G., Chiew, Y.W., Desaive, T., Ralib, A.M., Nor, M.B.M., 2018. Assessing mechanical ventilation asynchrony through iterative airway pressure reconstruction. Comput. Methods Programs Biomed. 157, 217–224.

Choo, J., 2018. Large deformation poromechanics with local mass conservation: An enriched Galerkin finite element framework. Internat. J. Numer. Methods Engrg. 116 (1), 66–90.

Coleman, B.D., 1964. Thermodynamics of materials with memory. Arch. Ration. Mech. Anal. 17 (1), 1–46.

Coleman, B.D., Gurtin, M.E., 1967. Thermodynamics with internal state variables. J. Chem. Phys. 47 (2), 597–613.

Concha, F., Hurtado, D.E., 2020. Upscaling the poroelastic behavior of the lung parenchyma: A finite-deformation micromechanical model. J. Mech. Phys. Solids 145, 104147.

Concha, F., Sarabia-Vallejos, M., Hurtado, D.E., 2018. Micromechanical model of lung parenchyma hyperelasticity. J. Mech. Phys. Solids 112, 126–144.

Coussy, O., 2004. Poromechanics. John Wiley & Sons.

Coussy, O., 2007. Revisiting the constitutive equations of unsaturated porous solids using a Lagrangian saturation concept. Int. J. Numer. Anal. Methods Geomech. 31 (15), 1675–1694.

Denny, E., Schroter, R., 2000. Viscoelastic behavior of a lung alveolar duct model. J. Biomech. Eng. 122 (2), 143–151.

Escolar, J.D., Escolar, A., 2004. Lung histeresis: a morphological view. Histol. Histopathol..

Fung, Y., 1988. A model of the lung structure and its validation. J. Appl. Physiol. 64 (5), 2132–2141.

Fung, Y.c.B., Patitucci, P., Tong, P., 1978. Stress and strain in the lung. J. Eng. Mech. Div. 104 (1), 201–223.

Gibson, G., Pride, N., 1976. Lung distensibility. The static pressure-volume curve of the lungs and its use in clinical assessment. Br. J. Dis. the Chest 70, 143–184.

Gil, J., Bachofen, H., Gehr, P., Weibel, E., 1979. Alveolar volume-surface area relation in air-and saline-filled lungs fixed by vascular perfusion. J. Appl. Physiol. 47 (5), 990–1001.

Goerke, J., 1998. Pulmonary surfactant: functions and molecular composition. Biochim. Biophys. Acta (BBA)- Mol. Basis Dis. 1408 (2–3), 79–89.

Griese, M., 1999. Pulmonary surfactant in health and human lung diseases: state of the art. Eur. Respir. J. 13 (6), 1455–1476.

Harris, R.S., 2005. Pressure-volume curves of the respiratory system. Respir. Care 50 (1), 78–99.

Hess, D.R., 2014. Respiratory mechanics in mechanically ventilated patients. Respir. Care 59 (11), 1773–1794.

Holzapfel, G.A., 2002. Nonlinear solid mechanics: a continuum approach for engineering science.

Hubmayr, R.D., 2002. Perspective on lung injury and recruitment: a skeptical look at the opening and collapse story. Am. J. Respir. Crit. Care Med. 165 (12), 1647–1653.

Hurtado, D.E., Avilés-Rojas, N., Concha, F., 2023. Multiscale modeling of lung mechanics: From alveolar microstructure to pulmonary function. J. Mech. Phys. Solids 105364.

Hurtado, D.E., Castro, S., Madrid, P., 2017a. Uncertainty quantification of 2 models of cardiac electromechanics. Int. J. Numer. Methods Biomed. Eng. 33 (12), e2894.

Hurtado, D.E., Villarroel, N., Andrade, C., Retamal, J., Bugedo, G., Bruhn, A.R., 2017b. Spatial patterns and frequency distributions of regional deformation in the healthy human lung. Biomech. Model. Mechanobiol. 16 (4), 1413–1423.

Hurtado, D.E., Zavala, P., 2021. Accelerating cardiac and vessel mechanics simulations : An energy-transform variational formulation for soft-tissue hyperelasticity. Comput. Methods Appl. Mech. Engrg. 379, 113764.

Ingenito, E.P., Tsai, L.W., Majumdar, A., Suki, B., 2005. On the role of surface tension in the pathophysiology of emphysema. Am. J. Respir. Crit. Care Med. 171 (4), 300–304.

Ismail, M., Comerford, A., Wall, W., 2013. Coupled and reduced dimensional modeling of respiratory mechanics during spontaneous breathing. Int. J. Numer. Methods Biomed. Eng. 29 (11), 1285–1305.

Jbaily, A., Frank, S., Szeri, A.J., 2020. Pulmonary mechanics and gas exchange: a mathematical framework. Internat. J. Engrg. Sci. 154, 103276.

Jonson, B., Svantesson, C., 1999. Elastic pressure–volume curves: what information do they convey? Thorax 54 (1), 82–87.

Knudsen, L., Ochs, M., 2018. The micromechanics of lung alveoli: structure and function of surfactant and tissue components. Histochem. Cell Biol. 150, 661–676.

Kralchevsky, P.A., Danov, K.D., Denkov, N.D., 1997. Chemical physics of colloid systems and interfaces. In: Handbook of surface and colloid chemistry, vol. 2, CRC Press LLS: Boca Raton.

Kylstra, J.A., Schoenfisch, W.H., 1972. Alveolar surface tension in fluorocarbon-filled lungs. J. Appl. Physiol. 33 (1), 32–35.

Laloui, L., Klubertanz, G., Vulliet, L., 2003. Solid-liquid-air coupling in multiphase porous media. Int. J. Numer. Anal. Methods Geomech. 27 (3), 183–206.

Lange, N.R., Schuster, D.P., 1999. The measurement of lung water. Crit. Care 3 (2), 19–24.

Levy, M.M., 2002. Optimal PEEP in ARDS: Changing concepts and current controversies. Crit. Care Clin. 18 (1), 15–33.

Li, C., Borja, R.I., Regueiro, R.A., 2004. Dynamics of porous media at finite strain. Comput. Methods Appl. Mech. Engrg. 193 (36–38), 3837–3870.

Logg, A., Mardal, K.A., Wells, G.N., et al., 2012. Automated Solution of Differential Equations by the Finite Element Method. Springer.

Lu, N., Zhang, C., 2019. Soil sorptive potential: Concept, theory, and verification. J. Geotech. Geoenvironmental Eng. 145 (4), 04019006.

Lubliner, J., 1973. On the structure of the rate equations of materials with internal variables. Acta Mech. 17 (1), 109–119.

Ma, B., Breen, B., Bates, J.H., 2013. Influence of parenchymal heterogeneity on airway-parenchymal interdependence. Respir. Physiol. Neurobiol. 188 (2), 94–101.

Ma, H., Fujioka, H., Halpern, D., Bates, J.H., Gaver III, D.P., 2023. Full-lung simulations of mechanically ventilated lungs incorporating recruitment/derecruitment dynamics. Front. Netw. Physiol. 3.
Ma, H., Fujioka, H., Halpern, D., Gaver III, D.P., 2020. Surfactant-mediated airway and acinar interactions in a multi-scale model of a healthy lung. Front. Physiol. 11, 941.
Manikantan, H., Squires, T.M., 2020. Surfactant dynamics: hidden variables controlling fluid flows. J. Fluid Mech. 892, P1.
Matamis, D., Lemaire, F., Harf, A., Brun-Buisson, C., Ansquer, J., Atlan, G., 1984. Total respiratory pressure-volume curves in the adult respiratory distress syndrome. Chest 86 (1), 58–66.
Maury, B., 2013. The Respiratory System in Equations. Springer-Verlag Italia.
Mead, J., Whittenberger, J., Radford Jr., E., 1957. Surface tension as a factor in pulmonary volume-pressure hysteresis. J. Appl. Physiol. 10 (2), 191–196.
Mergoni, M., Martelli, A., Volpi, A., Primavera, S., Zuccoli, P., Rossi, A., 1997. Impact of positive end-expiratory pressure on chest wall and lung pressure–volume curve in acute respiratory failure. Am. J. Respir. Crit. Care Med. 156 (3), 846–854.
Middleton, S., Dimbath, E., Pant, A., George, S.M., Maddipati, V., Peach, M.S., Yang, K., Ju, A.W., Vahdati, A., 2022. Towards a multi-scale computer modeling workflow for simulation of pulmonary ventilation in advanced COVID-19. Comput. Biol. Med. 145, 105513.
Morris, J., Ingenito, E., Mark, L., Kamm, R., Johnson, M., 2001. Dynamic behavior of lung surfactant. J. Biomech. Eng. 123 (1), 106–113.
Morton, S.E., Dickson, J., Chase, J.G., Docherty, P., Desaive, T., Howe, S.L., Shaw, G.M., Tawhai, M., 2018. A virtual patient model for mechanical ventilation. Comput. Methods Programs Biomed. 165, 77–87.
Neelakantan, S., Xin, Y., Gaver, D.P., Cereda, M., Rizi, R., Smith, B.J., Avazmohammadi, R., 2022. Computational lung modelling in respiratory medicine. J. R. Soc. Interface 19 (191), 20220062.
v. Neergaard, K., 1929. Neue Auffassungen über einen Grundbegriff der Atemmechanik: Die Retraktionskraft der Lunge, abhängig von der Oberflächenspannung in den Alveolen. Z. Gesamte Exp. Med. 66 (1), 373–394.
Nikooee, E., Habibagahi, G., Hassanizadeh, S.M., Ghahramani, A., 2013. Effective stress in unsaturated soils: A thermodynamic approach based on the interfacial energy and hydromechanical coupling. Transp. Porous Media 96, 369–396.
Otis, D.R., Ingenito, E.P., Kamm, R.D., Johnson, M., 1994. Dynamic Surface-Tension of Surfactant Ta - Experiments and Theory. J. Appl. Physiol. 77 (6), 2681–2688.
Patte, C., Genet, M., Chapelle, D., 2022. A quasi-static poromechanical model of the lungs. Biomech. Model. Mechanobiol. 21 (2), 527–551.
Pattle, R., 1955. Properties, function and origin of the alveolar lining layer. Nature 175 (4469), 1125–1126.
Pozin, N., Montesantos, S., Katz, I., Pichelin, M., Vignon-Clementel, I., Grandmont, C., 2017. A tree-parenchyma coupled model for lung ventilation simulation. Int. J. Numer. Methods Biomed. Eng. 33 (11), e2873.
Quiros, K., Nelson, T., Sattari, S., Mariano, C., Ulu, A., Dominguez, E., Nordgren, T., Eskandari, M., 2022. Mouse lung mechanical properties under varying inflation volumes and cycling frequencies. Sci. Rep. 12 (1), 7094.
Raghavendran, K., Willson, D., Notter, R., 2011. Surfactant therapy for acute lung injury and acute respiratory distress syndrome. Crit. Care Clin. 27 (3), 525–559.
Retamal, J., Hurtado, D.E., Villarroel, N., Bruhn, A., Bugedo, G., Amato, M.B.P., Costa, E.L.V., Hedenstierna, G., Larsson, A., Borges, J.B., 2018. Does Regional Lung Strain Correlate With Regional Inflammation in Acute Respiratory Distress Syndrome During Nonprotective Ventilation? An Experimental Porcine Study. Crit. Care Med. 46 (6), 591–599.
Roth, C.J., Ismail, M., Yoshihara, L., Wall, W.A., 2017. A comprehensive computational human lung model incorporating inter-acinar dependencies: Application to spontaneous breathing and mechanical ventilation. Int. J. Numer. Methods Biomed. Eng. 33 (1), e02787.
Scarpelli, E.M., 1977. The surfactant system of the lung. Int. Anesthesiol. Clin. 15 (4), 19–60.
Schürch, S., Bachofen, H., Goerke, J., Green, F., 1992. Surface properties of rat pulmonary surfactant studied with the captive bubble method: adsorption, hysteresis, stability. Biochim. Biophys. Acta (BBA)- Biomembr. 1103 (1), 127–136.
Smith, J.C., Stamenovic, D., 1986. Surface forces in lungs. I. Alveolar surface tension-lung volume relationships. J. Appl. Physiol. 60 (4), 1341–1350.
Steimle, K.L., Mogensen, M.L., Karbing, D.S., de la Serna, J.B., Andreassen, S., 2011. A model of ventilation of the healthy human lung. Comput. Methods Programs Biomed. 101 (2), 144–155.
Suki, B., Stamenovic, D., Hubmayr, R., 2011. Lung parenchymal mechanics. Compr. Physiol. 1 (3), 1317.
Sun, W., Ostien, J.T., Salinger, A.G., 2013. A stabilized assumed deformation gradient finite element formulation for strongly coupled poromechanical simulations at finite strain. Int. J. Numer. Anal. Methods Geomech. 37 (16), 2755–2788.
Suter, P.M., Fairley, H.B., Isenberg, M.D., 1975. Optimum end-expiratory airway pressure in patients with acute pulmonary failure. N. Engl. J. Med. 292 (6), 284–289.
Takeuchi, M., Sedeek, K.A., Schettino, G.P., Suchodolski, K., Kacmarek, R.M., 2001. Peak pressure during volume history and pressure–volume curve measurement affects analysis. Am. J. Respir. Crit. Care Med. 164 (7), 1225–1230.
Tawhai, M.H., Nash, M.P., Lin, C.L., Hoffman, E.A., 2009. Supine and prone differences in regional lung density and pleural pressure gradients in the human lung with constant shape. J. Appl. Physiol. 107 (3), 912–920.
The CGAL Project, 2021. CGAL User and Reference Manual, 5.3.1 ed. CGAL Editorial Board, URL: https://doc.cgal.org/5.3.1/Manual/packages.html.
Vandamme, M., Brochard, L., Lecampion, B., Coussy, O., 2010. Adsorption and strain: the CO2-induced swelling of coal. J. Mech. Phys. Solids 58 (10), 1489–1505.
Veldhuizen, R., Nag, K., Orgeig, S., Possmayer, F., 1998. The role of lipids in pulmonary surfactant. Biochim. Biophys. Acta (BBA)- Mol. Basis Dis. 1408 (2–3), 90–108.
Venegas, J.G., Harris, R.S., Simon, B.A., 1998. A comprehensive equation for the pulmonary pressure-volume curve. J. Appl. Physiol. 84 (1), 389–395.
Vuong, A.T., Yoshihara, L., Wall, W., 2015. A general approach for modeling interacting flow through porous media under finite deformations. Comput. Methods Appl. Mech. Engrg. 283, 1240–1259.
West, J.B., 2012. Respiratory Physiology: The Essentials, ninth ed. Lippincott Williams & Wilkins.
Wilson, T.A., 1982. Surface tension-surface area curves calculated from pressure-volume loops. J. Appl. Physiol. 53 (6), 1512–1520.
Zhang, Y., 2018. Mechanics of adsorption–deformation coupling in porous media. J. Mech. Phys. Solids 114, 31–54.
Zhang, Z., Xu, S., Ren, W., 2014. Derivation of a continuum model and the energy law for moving contact lines with insoluble surfactants. Phys. Fluids 26 (6).
Zhao, Q., Ren, W., Zhang, Z., 2021. A thermodynamically consistent model and its conservative numerical approximation for moving contact lines with soluble surfactants. Comput. Methods Appl. Mech. Engrg. 385, 114033.
Zhou, C., Chase, J.G., Knopp, J., Sun, Q., Tawhai, M., Möller, K., Heines, S.J., Bergmans, D.C., Shaw, G.M., Desaive, T., 2021. Virtual patients for mechanical ventilation in the intensive care unit. Comput. Methods Programs Biomed. 199, 105912.